Journal of Nanobiotechnology

RESEARCH Open Access

Microneedle-delivered ROS-adaptive asiatic acid nanoparticles promote scarless repair via remodeling the pathological microenvironment

Yawen Zhang[1], Xuanyu Tang[1], Yijing Ma[1], Yi Qiu[1], Xiaoting Wu[1], Yue Wu[1], Lulu Zeng[1], Lingfeng Chen[1], Haibin Wu[1], Yanyan Zheng[2], Jing Xie[2*], Guang Liang[1*] and Lina Yin[1*]

Abstract

Hypertrophic scar (HS) is a pathologic fibrotic disease caused by aberrant wound healing following severe skin injury. Despite advances in clinical treatments, the therapeutic outcomes remain suboptimal, mainly due to inadequate penetration through the thickened stratum corneum barrier and insufficient site-specific drug delivery within the lesional tissue. To address these limitations, we developed a hyaluronic acid-based dissolving microneedle array loaded with reactive oxygen species (ROS)-responsive asiatic acid nanoparticles (AA/PTP MN). This advanced platform facilitates direct intradermal delivery of therapeutic agents by penetrating the stratum corneum. Upon dissolution in the scar tissue, the released AA/PTP nanoparticles respond to the elevated ROS levels, enabling precise and sustained release of asiatic acid (AA) to actively remodel the pathological microenvironment. This innovative nano-micro platform exhibited excellent ROS sensitivity, robust mechanical properties, and good biocompatibility. In vitro experiments revealed that AA/PTP can specifically inhibited the proliferation of hypertrophic scar fibroblasts and reduced macrophage migration. In the rabbit ear HS model, AA/PTP MN treatment effectively remodeled the pathological HS microenvironment, as evidenced by significantly reduced scar thickness, normalized collagen architecture, and marked inhibition of skin fibrosis. RNA sequencing analysis confirmed that this therapeutic effect was achieved through multi-faceted regulation of the scar microenvironment: inhibiting fibroblast and keratinocyte proliferation, attenuating inflammation, and reducing excessive collagen deposition. In summary, this microneedle-based strategy of microenvironment-specific drug release represents a promising and effective therapeutic avenue for achieving scarless regeneration in hypertrophic scars.

*Correspondence:
Jing Xie
christian_xj@163.com
Guang Liang
wzmcliangguang@163.com
Lina Yin
lnyin@hmc.edu.cn

Full list of author information is available at the end of the article

Keywords Hypertrophic scar, Dissolving microneedles, Asiatic acid, Reactive oxygen species (ROS), Nano-micro platform

Graphical abstract

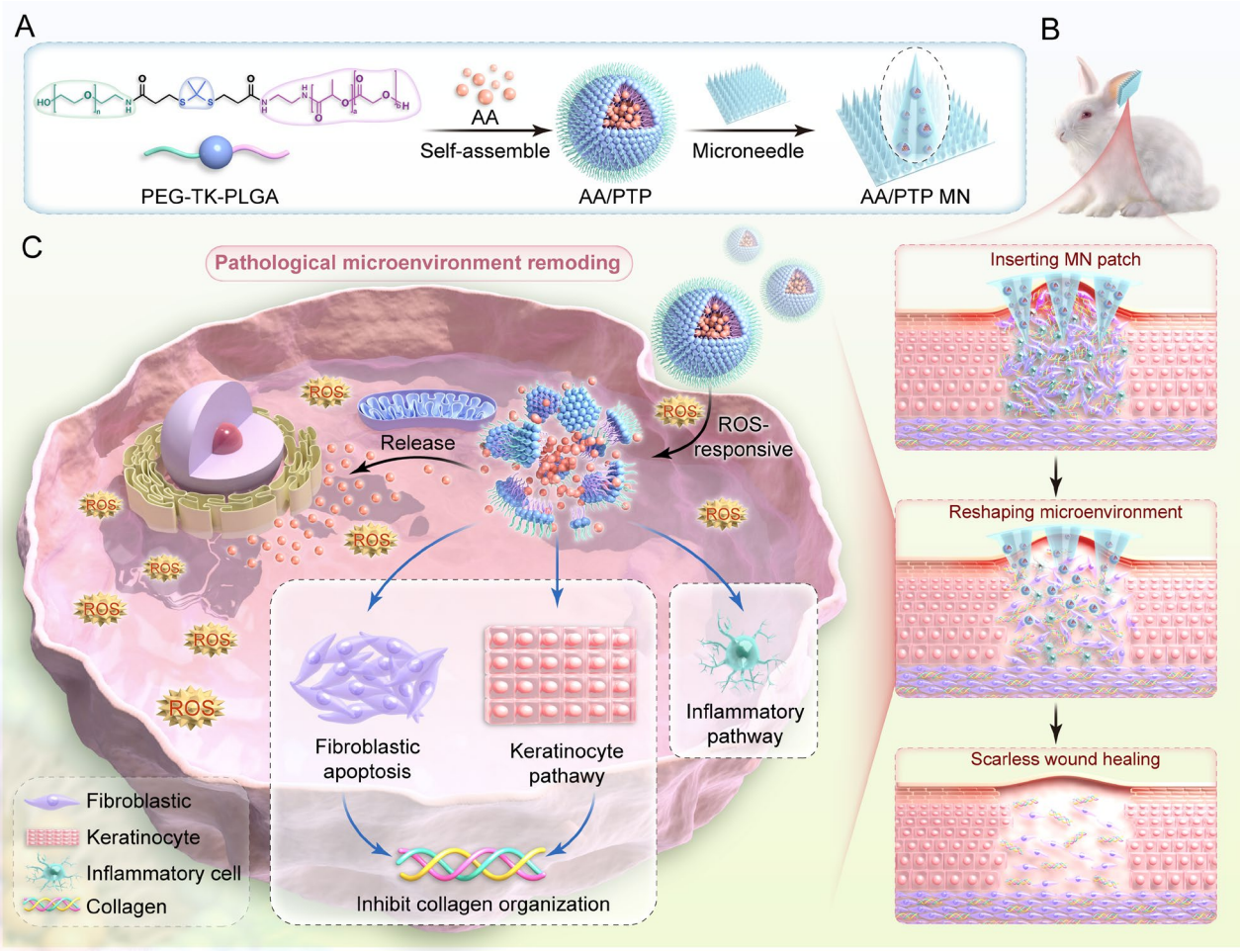

Introduction

Hypertrophic scar (HS) is a dysfunctional fibrotic proliferation resulting from various forms of skin trauma, leading to both physical disfigurement and significant psychological distress for patients [1]. The formation of HS is influenced by multiple factors, including excessive fibroblast proliferation and differentiation, abnormal collagen deposition, and dysregulated inflammatory responses [2, 3]. Conventional treatments for HS primarily involve surgical excision, cryotherapy, laser therapy, and local intralesional injections of glucocorticoids, steroids, or 5-fluorouracil [4, 5]. However, these approaches are often associated with drawbacks, including high recurrence rates, prolonged healing times, and substantial side effects [6–8]. Accordingly, it is essential to develop novel and more effective anti-scar therapies.

Asiatic acid (AA), the primary active ingredient of the herbal medicine *Centella asiatica* (CA) [9, 10], has demonstrated therapeutic potential in various dermatological diseases [11, 12], including psoriasis [13], ultraviolet-A induced photoaging [14], and skin cancers [15]. Its mechanisms of action include promoting extracellular matrix remodeling, inhibiting inflammation, stimulating angiogenesis, and regulating oxidative stress. Furthermore, AA has been shown to exert a potent inhibitory effect on fibrocyte proliferation [16, 17]. Based on these properties, AA has emerged as a promising candidate for HS. Nevertheless, its clinical application is hindered by challenges such as low water solubility, rapid systemic clearance, and poor bioavailability [18]. To address these limitations, AA has been formulated into various nanoparticle (NPs) systems [17, 19]. However, there remain some critical challenges with conventional NPs in the treatment of HS: (1)

While NPs can enhance drug absorption, they often lack the ability to achieve targeted drug release at the lesion site, potentially leading to increased side effects; (2) The majority of NPs struggle to penetrate deeper regions of HS due to the stratum corneum barrier, potentially limiting their therapeutic efficacy. Consequently, it is desirable to construct a controlled-release drug platform with high selectivity, minimal side effects, responsiveness to endogenous stimuli, and enhanced tissue penetration.

In the HS microenvironment, excessive fibroblast proliferation and microvascular occlusion lead to localized hypoxia, which ultimately results in an abnormal increase in reactive oxygen species (ROS) [20, 21]. The thioketal (TK) bond, a ROS-sensitive covalent bond, degrades into acetone and thiols even at low ROS concentrations [22] and has been used for controlled release delivery of therapeutic drugs for tumors and inflammatory diseases. In this study, we incorporated TK bonds between polyethylene glycol (PEG) and polylactic glycolic acid (PLGA), enabling the formation of self-assembling nanoparticles and further encapsulating AA (AA/PTP). The prepared AA/PTP NPs were designed to be cleaved by ROS in the HS microenvironment, facilitating the responsive release of AA at the target region and reducing side effects, positioning AA/PTP as a promising targeted delivery system for therapeutic applications.

Another challenge limiting the efficacy of NPs for HS treatment is the presence of specialized skin barriers, such as the stratum corneum and the dense structure of scar tissue, which significantly impede drug penetration [23, 24]. However, advancements in nano/micro fabrication have led to the development of a novel and promising transdermal delivery method based on microneedle (MN) technology, which has revolutionized the treatment of various skin diseases [25, 26]. They can bypass the stratum corneum by creating microchannels through micrometer-sized needle tips, enabling the convenient, noninvasive, and painless delivery of therapeutic molecules directly into the dermis and subsequently enter the circulatory system [27–29]. Furthermore, researchers have demonstrated that microneedle devices enable the modulation of tissue ultrastructure and biomechanical properties by penetrating the epidermis and forming microporous array channels, thereby achieving scarless healing in a minimally invasive manner [30].

Herein, we developed endogenous ROS-responsive nanoparticles and incorporated them into a hyaluronic acid-based dissolving microneedle array (AA/PTP MN) to facilitate more efficient and painless therapy for HS (as illustrated in Scheme 1). The AA/PTP MN patch was applied to HS tissue, where the microneedle tips created microchannels, facilitating intradermal deposition of AA/PTP nanoparticles as the microneedle matrix dissolved. Subsequently, in the high-ROS microenvironment, AA was targeted released due to the unique structural properties of AA/PTP. The therapeutic mechanism of AA/PTP MN in treating HS may be related to the inhibition of abnormal fibroblast and keratinocyte proliferation in HS tissue, as well as the alleviation of inflammatory responses. Overall, functional transdermal nano-microneedles that respond to pathological microenvironments enhance drug delivery efficacy while minimizing potential adverse effects.

Experimental section

Materials, cell lines, and animals

The reagents and materials were sourced as follows: AA (98% purity) was produced by Guangxi Institute for Food and Drug Control (Nanning, China). PEG_{2000}-TK-$PLGA_{5000}$ were acquired from Xi'an Ruixi Biotechnology (Xi'an, China). Coumarin 6 (C6) was obtained from Dalian Meilun Biotechnology Co., Ltd. (Liaoning, China). The Cell Counting Kit-8 (CCK-8) and crystal violet were obtained from Beyotime (China). Small molecular Hyaluronic acid (HA, 1000 Da) was purchased from Shanghai Yuanye Bio-Technology Co., Ltd. (Shanghai, China). Polydimethylsiloxane (PDMS) was bought from Taizhou Microchip Medical Technology Co., Ltd. (Taizhou, China). All supplementary reagents and solvents utilized were of analytical purity.

In compliance with the Declaration of Helsinki and with approval from Wenzhou People's Hospital (Approval No. 2022 – 415), primary hypertrophic scar fibroblasts (HSFb) and normal dermal fibroblasts (HDF) were isolated from fresh human pathological HS tissues and normal skin, respectively. The procedure was conducted as follows: the surgically harvested dermal specimens were thoroughly cleaned with sterile PBS and then sliced into tiny pieces. Following the removal of attached fat, the tissue fragments were digested with collagenase type I (BioFroxx, Germany) for 6 h. Isolated cells were cultured in high glucose DMEM (HyClone, South Logan, USA) containing 10% fetal bovine serum (Gibco, USA) and 1% penicillin/streptomycin at 37 °C. For in vitro experiments, cells between passages three and seven were used. The HaCaT cell line was purchased from Meisen Cell Technology (Zhejiang, China).

Female New Zealand rabbits (weighing between 1.5 and 2.0 kg, single-housed) and Sprague-Dawley (SD) rats (200 ± 20 g) were procured from Zhejiang Laboratory Animal Center (Hangzhou, China). All animal care procedures and experimental protocols were conducted under the guidelines established by the Animal Ethics Committee of Zhejiang Province (Approval No. 2021 – 266).

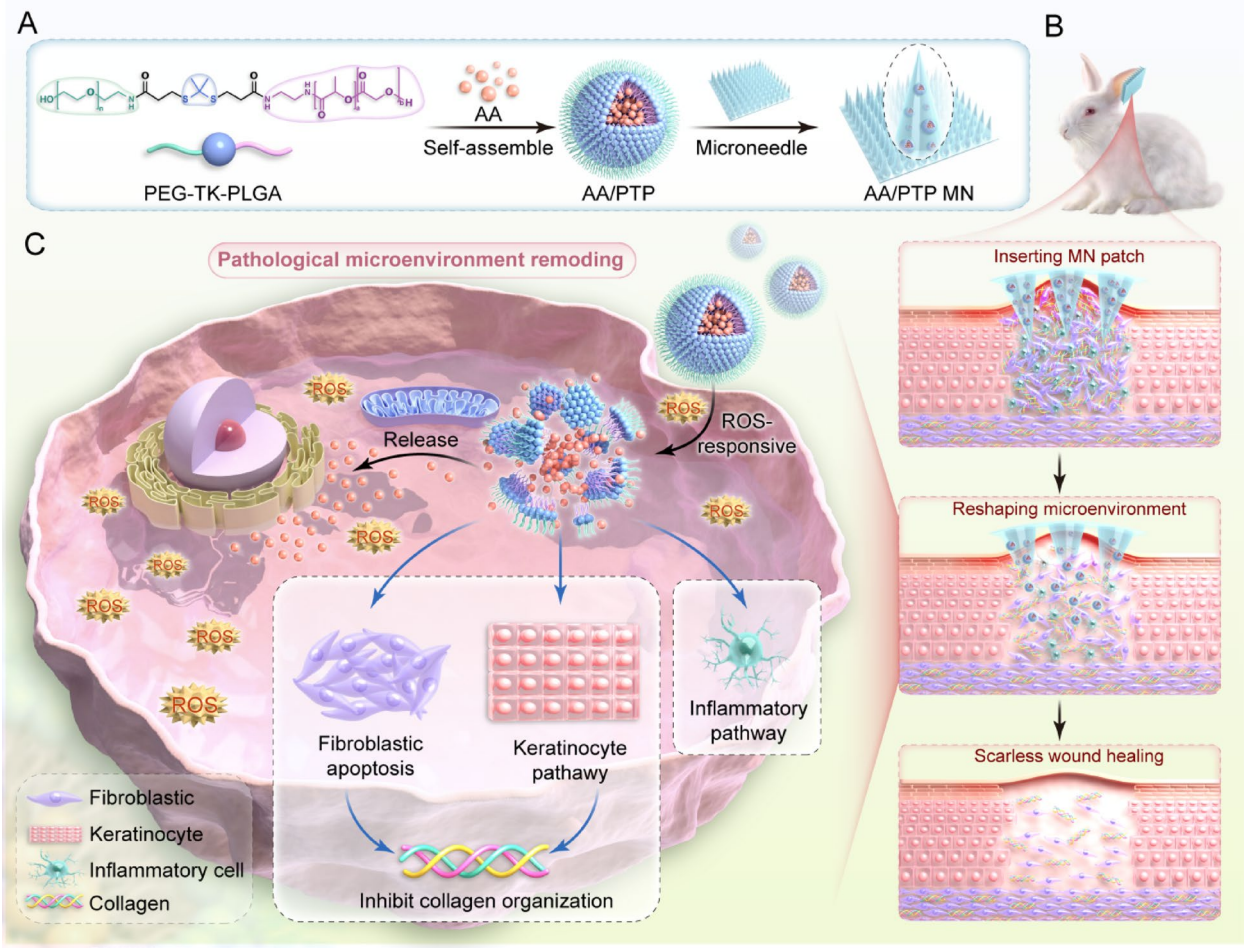

Fig. 1 Schematic illustration of the AA/PTP MN platform. (**A**) Diagram of the nano-microneedle fabrication process. (**B**) Schematic illustration of AA/PTP MN on HS treatment. The MN patch penetrates the HS tissue, and AA/PTP nanoparticles are released as the microneedle matrix dissolves. Subsequently, the TK bond breaks in a high-ROS microenvironment, and AA/PTP efficiently decomposes and targeted releases the drug due to its unique structure. (**C**) During this process, fibroblast apoptosis and keratinocyte rearrangement are induced, ROS levels and inflammation are reduced, leading to inhibition of collagen synthesis and effective treatment of HS

Preparation and characterization of AA/PEG_{2000}-TK-$PLGA_{5000}$ nanoparticle

AA/PEG_{2000}-TK-$PLGA_{5000}$ NPs (AA/PTP) were synthesized using a self-assembly emulsion method. Briefly, PEG_{2000}-TK-$PLGA_{5000}$ (600 mg) and AA (50 mg) were dissolved in 10 mL of acetone and 5 mL of methanol, respectively. Subsequently, these two solutions were thoroughly mixed and then added to 150 mL of 0.5% tocofersolan (w/v) and magnetically stirred at room temperature (10 min, 800 rpm). The organic solvent was removed via rotary evaporation, and any residual material was separated by centrifugation (10 min, 3000 rpm). Finally, the nanoparticle dispersion was collected for further use.

The morphology of AA/PTP was photographed using transmission electron microscopy (TEM, FEI Tecnai F30, USA), while the size distribution and ζ potential were measured via a Malvern Zetasizer Nano ZS90.

The AA content in both the AA/PTP complex and the release samples was quantified using a Shimadzu HPLC system (LC-20AD, Japan) [17, 19]. The chromatographic eluent system was composed of KH_2PO_4 (pH 3.0) mixed with acetonitrile/methanol (1:1) in a 20:80 (v/v) ratio, isocratically delivered at 1.0 mL/min. The detection wavelength of AA was 210 nm. Prior to analysis, the AA/PTP dispersion was diluted with DMSO and subjected to 10 min of ultrasonication, followed by filtration. The resulting filtrate was then analyzed by HPLC. The following equations were used to calculate the drug loadings (DL, %) and encapsulation efficiency (EE, %) of AA.

$$\mathrm{EE}(\%)=\frac{\text{Amount of AA in AA/PTP}}{\text{Total AA added}}\times 100\% \quad (1)$$

$$\mathrm{DL}(\%)=\frac{\text{Amount of AA in AA/PTP}}{\text{Weight of AA/PTP}}\times 100\% \quad (2)$$

The in vitro release profile of AA/PTP was performed using dialysis technique under varying H_2O_2 concentrations. 1 mL of AA/PTP dispersion was placed inside a dialysis bag (7000 Da) and submerged in 20 mL of pH 7.4 PBS containing H_2O_2 (0, 0.05, 0.5 and 5 mM). The dialysis bag was then agitated at 100 rpm and maintained at 37 °C. At predetermined time intervals (0.5, 1, 2, 3, 4, 6, 8, 10, 12, 24, and 48 h), samples of the release medium were collected, and the entire medium was replaced with fresh PBS. The cumulative release of AA was quantified by HPLC as previously mentioned.

Fluorescently labeled NPs were produced by substituting C6 for AA, which was used in the cell uptake experiment (C6/PTP).

Preparation and characterization of MNs

Fabrication of AA/PTP MN patches

Conical hyaluronic acid (HA) MN was prepared using PDMS female molds (10 mm square array with a 10 × 10 needle configuration, where each needle measured 800 μm in height, 200 μm in base diameter, and 700 μm in pitch). The preparation process began by combining either AA or a freeze-dried AA/PTP powder (containing 2 mg of AA) with 0.3 g of HA in deionized water to form a nanoplex-containing matrix solution. Subsequently, 250 μL of this matrix solution was carefully added to the mold. The PDMS mold was then centrifuged for 15 min at 3500 rpm to ensure complete infiltration of the biopolymer solution into the pyramidal cavities of the mold. The mold surface was cleaned of excess solution. Following this, the AA/PTP MN patches were gently slipped off the mold after drying and solidifying.

Fluorescently labeled microneedle patches (C6-labeled nanoparticles and rhodamine B-labeled microneedle matrix) were prepared to observe the morphology of microneedles and the skin penetration experiment on rabbit ear scar tissue. Furthermore, the amounts of AA in AA MN patch and AA/PTP MN patch were quantified by the HPLC method described previously.

Analysis of morphology, mechanical properties, and dissolvability

The morphology of the AA/PTP MN was examined by a focused ion beam-scanning electron microscope (FIB-SEM, FEI Scios 2 HiVac, Thermo Scientific, USA) and a confocal laser scanning microscope (CLSM, A1 HD25, Nikon, Japan).

The biomechanical performance of the AA/PTP MN was quantitatively assessed in a texture analyzer (TMS-PRO, Food Technology Corporation, USA). The test was conducted with a trigger force of 0.05 N and a TMS 10 mm cylindrical light-metal probe. The AA/PTP MN was secured to the platform with the needle tips positioned toward the pressure sensor. The sensor was programmed to move at a constant speed of 0.5 mm/s. Measurement commenced when the needle tips touched the sensor and concluded once 80% of the predefined displacement (640 μm) was achieved. Throughout the procedure, both the displacement distance and the compressive force were continuously recorded.

To monitor the dissolving process, the AA MN and AA/PTP MN patches with different hyaluronic acid matrix ratios (10%HA、20%HA、25%HA、30%HA) were pressed onto the rabbit ear and subsequently removed at different time points. The morphological changes of the retrieved microneedles were observed using a scanning electron microscope (SEM, IT200, JEOL, Japan) or an optical microscope.

Hemolysis experiment

For hemocompatibility assessment, freshly isolated rabbit erythrocytes were reconstituted in normal saline to a 2% (v/v) concentration and then combined with an equal volume of an AA/PTP saline solution. Furthermore, the negative and positive controls were prepared by mixing the erythrocyte suspension with normal saline and water, respectively. Following a two-hour incubation at 37 °C, the mixtures were centrifuged at 12,000 rpm. The obtained supernatant was spectrophotometrically quantified by a Synergy2 microplate reader (Bio-Tek, USA) at 541 nm. Equation 3 was used to calculate the hemolysis ratio.

$$\text{Hemolysis ratio}(\%)=\frac{\text{Abs sample - Abs negative}}{\text{Abs positive - Abs negative}}\times 100\% \quad (3)$$

The absorbances of the AA/PTP sample, positive control and negative control are denoted as Abs_{sample}, $Abs_{positive}$ and $Abs_{negative}$, respectively. Each group comprised three replicates.

In vivo investigation of AA/PTP MN insertion

To visualize the transdermal penetration of AA/PTP MN and the drug distribution in local skin tissue, C6-labeled microneedles were applied to the HS tissue of rabbit ears for 10 min and subsequently removed. As a contrast, C6/PTP was applied directly to the HS tissue. After 1 h, the skin tissues were carefully excised and snap-frozen in liquid nitrogen. Subsequently, samples were sectioned using a cryostat microtome (HM525NX, Thermo Scientific, USA) and stained with DAPI nuclear dye. The prepared sections were subjected to fluorescence visualization under a BX53 fluorescence microscope (Olympus, Japan) equipped with a PANNORAMIC SCAN II imaging system (3D HISTECH Ltd) to confirm the effective insertion of the microneedles.

Optical coherence tomography (OCT, TowardPi Medical Technology Ltd, China) was employed to

quantitatively assess the penetration depth of AA/PTP MN in rabbit ear HS tissue. The insertion process was imaged in real time using an OCT system at a laser wavelength of 1060 nm.

In vitro cell viability

To evaluate the viability, HSFb and Raw 264.7 cells were seeded at a density of 5×10^3 cells per well in 96-well plates and incubated overnight. Thereafter, the cells were exposed to gradient concentrations of free AA or AA/PTP solution (2, 5, 10, 20, 50, and 100 μM). After 24 h of incubation, CCK-8 reagent (10 μL) was added and cultured for an additional hour. The OD450 values were then measured by a microplate reader. Untreated HSFb and Raw 264.7 cells were used as the control, representing 100% cell viability.

In vitro apoptosis properties of AA/PTP

The apoptotic effect of AA/PTP on HSFb was determined by the Annexin V-APC/PI apoptosis detection kit (Multi Sciences, China). Specifically, HSFb were seeded at a density of 1×10^5 cells per well in 12-well plates and cultured overnight. Subsequently, various formulations at 5 or 10 μM were applied to the cells. After a 24-hour incubation period, the cells were washed and stained in the dark for 10 min with annexin V-APC (2 μL) and propidium iodide (PI, 4 μL). The samples were analyzed using a flow cytometer (BD Accuri C6 Plus, BD Biosciences, USA), and the resulting data were processed with FlowJo V10 software (TreeStar Inc., USA).

Cellular uptake

Due to the stable properties and high fluorescence efficiency, C6 was employed as the fluorescent indicator for cellular uptake investigations. HSFb and Raw 264.7 cells were seeded at a density of 5×10^4 cells per well in 6-well plates and cultured for 12 h. Thereafter, C6-labeled NPs (C6/PTP, 2 μg/mL) were added and co-incubated for different times. The cells were gathered for flow cytometric quantitative analysis following a thorough PBS wash to eliminate uninternalized C6/PTP. For nanoscale localization profiling, cell monolayers were dual-stained with DAPI and Lysotracker Red, respectively. Finally, intracellular fluorescence was visualized using a fluorescence microscope (EVOS M7000, Invitrogen, USA).

Cell migration and intracellular ROS measurement

Wound scratch assays were used to evaluate HSFb migration in the presence of AA and AA/PTP. HSFb were seeded into 6-well plates (3×10^5 cells/well) and allowed to adhere for 12 h. Uniform scratches were created in the middle of the wells using sterile pipette tips. Fresh medium containing AA or AA/PTP was added to each well. Cell migration was monitored at 0, 6, 12, and 24 h using inverted microscopy. Quantitative analysis was performed by measuring scratch areas with ImageJ software. The wound healing rate (WHR) was determined using Eq. 4:

$$\mathrm{WHR}(\%) = \frac{\mathrm{A\,0\text{-}A\,t}}{\mathrm{A0}} \times 100\% \tag{4}$$

Where A_0 and A_t represent the area of the scratch at 0 h and t h, respectively.

The elimination of intracellular ROS was monitored by 2'–7'-dichlorofluorescindiacetate (DCFH-DA; Solarbio Science & Technology, China) in HSFb, HDF, and HaCaT cell lines. Specifically, three cell lines were seeded in 12-well plates (2×10^5 cells/well) and incubated with different interventions (AA and AA/PTP) and H_2O_2 (200 μM). After 12 h of culture, cells were washed with cold PBS and incubated with DCFH-DA (10 μM) for 30 min at 37 ℃ in the dark. Untreated cells were used as the control group. Subsequently, cells were evaluated using fluorescence microscopy. The mean fluorescence intensity (MFI) was semiquantified using ImageJ software (NIH, USA).

Migration and polarization of macrophages

To simulate the recruitment of immune cells to HS tissues, a transwell assay was used to evaluate the chemotactic migration ability of macrophages. Raw 264.7 (1×10^5 cells/well) were inoculated into the upper chamber of a 3 μm pore size transwell insert (Corning, USA), and the lower chamber was filled with HSFb culture supernatant (0.22 μm filtrate). After 24 h incubation with AA or AA/PTP (5, 10 μM) at 37 °C, migrated cells on the lower side of the insert were fixed with 4% formalin and stained with crystal violet. The stained cells were observed and photographed with an inverted microscope.

To evaluate the anti-inflammatory activity of AA/PTP, we examined its effect on macrophage polarization from the pro-inflammatory M1 phenotype to the anti-inflammatory M2 phenotype. Briefly, Raw 264.7 cells were seeded in 6-well plates (2×10^5 cells/well) and incubated at 37 ℃ in 5% CO_2. Cells were then stimulated with LPS (500 ng/mL) in the presence of AA or AA/PTP for 24 h. Next, the cells were harvested, washed three times with PBS, and stained with anti-CD86-V450 (Thermo Fisher Scientific, USA), anti-CD206-APC (Liankebio, China), CD11b-FITC (Liankebio, China), and F4/80-PE (Liankebio, China), respectively. Finally, cells were resuspended in PBS and analyzed by flow cytometry (BD FACSCelesta, BD Biosciences, USA).

Pharmacodynamics studies

The HS model was surgically induced on the ventral surface of rabbit ears to evaluate the therapeutic efficacy of

microneedles in vivo. Briefly, New Zealand rabbits were anesthetized via intravenous injection into the ear using Zoletil 50 (0.15 mL/kg) and Su Mian Xin II (0.05 mL/kg). Three circular injuries (10 mm in diameter) were created per ear through complete excision of epidermis, dermis, and perichondrium, while avoiding damage to the central auricular artery and peripheral auricular veins. After a week, the newly formed scar tissue was peeled off to re-expose the wound, promoting accelerated granulation and fibroplasia. Following 21 days of recovery and epithelialization, firm and compact hypertrophic scars were formed at the wound sites. The rabbits were divided into 7 groups at random: normal group (untreated), HS model group (untreated), HS + Blank MN group, HS + AA/PTP group, HS + AA MN group, HS + AA/PTP MN group, and HS + CA Cream group (treated with *Centella asiatica* cream, a commercial product). Except for the normal and HS model groups, all other groups were treated once every other day ($n = 6$ per group). For the MN groups, the microneedle patches were applied to the scar sites and pressed firmly for 10 min. For the AA/PTP and CA Cream groups, the formulations were applied directly to the wound sites. After three weeks of continuous treatment, lesional tissues were harvested for morphological observation, histological examination, and protein expression analysis.

Efficacy assessment and histological analysis

After harvesting and fixing in 4% paraformaldehyde, the HS samples were embedded in paraffin and sectioned into 5 μm slices. The extent of re-epithelialization and collagen deposition was examined using hematoxylin and eosin (H&E) staining and Masson's trichrome staining, respectively. The stained sections were visualized using a fully automated digital slide scanner (Eclipse E100, Nikon). The scar elevation index (SEI) was obtained using Eq. 5, which represents the proportion between the thickness of hypertrophic scar tissue (H_{scar}) and normal tissue (H_{normal}) above the cartilage surface.

$$\mathrm{SEI}(\%) = \frac{\mathrm{H\ scar}}{\mathrm{H\ normal}} \tag{5}$$

For the immunohistochemical experiment, tissue sections were incubated with primary antibodies against collagen I (Proteintech, 1:1000), collagen III (Proteintech, 1:1000), α-smooth muscle actin (α-SMA) (Haoke Biotechnology, 1:2500), Cytokeratin 6 (CK6) (Biolynx Biotechnology, 1:2500) at 4 °C overnight. Subsequently, the sections were incubated with an HRP-conjugated secondary antibody (Haoke Biotechnology) for one hour at 25 °C. Following this, the sections were counterstained with hematoxylin. Positive cells were visualized by the application of DAB (3,3'-diaminobenzidine) to the sections.

Real-time polymerase chain reaction analysis (RT-PCR)

The expression of collagen and inflammatory factor genes in cells and rabbit ear tissues was analyzed using RT-PCR. Total mRNA was extracted and purified using the SteadyPure RNA Extraction Kit (Accurate Biotechnology (Hunan) Co., Ltd.), which was subsequently detected by a NanoDrop2000 micro-spectrophotometer (Thermo Scientific, Waltham, USA). The gene expression levels of collagen I (COL I), collagen III (COL III), transforming growth factor-beta1 (TGF-β1), interleukin-6 (IL-6), and interleukin-1β (IL-1β) were quantified through SYBR-based quantitative PCR (Yeasen Biotech Co., Ltd., China) on a BIO-RAD My Cycler (Germany). The comparative $2^{-\triangle\triangle Ct}$ method was used to evaluate the data. The oligonucleotide primer sequences that were utilized for PCR amplification are listed in Table S1.

RNA sequencing analysis

To investigate the RNA changes induced by various treatments on HS, RNA sequencing was performed on rabbit HS ear tissue from three experimental groups (normal, HS model, and HS + AA/PTP MN). Total RNA was extracted using Invitrogen TRIzol Reagent (Carlsbad, USA) and then assessed using a NanoDrop ND-1000 spectrophotometer (Wilmington, USA) and a Fragment Analyzer (Thermo Scientific, Waltham, USA). Subsequently, mRNA was purified and enriched using magnetic beads conjugated with Oligo(dT). Sequencing was conducted on the DNBSEQ platform using the PE150 model (Beijing Genomics Institute, Shenzhen, China). HISAT2 (version 2.2.1) and Bowtie2 (version 2.3.4.3) were used to map the clean reads to the genome and reference gene, respectively. RSEM (version 1.2.28) was used to quantify gene expression, and pheatmap (version 1.0.10) was used to draw the clustering heatmap of gene expression across different samples. Differential gene expression analysis was performed using DESeq2 (version 1.40.2), with a Q-value threshold of ≤ 0.05. Differentially expressed genes (DEGs) were identified using the following criteria: |fold change| ≥ 1.5 and $Q < 0.05$. Pathway enrichment analysis was performed using the Kyoto Encyclopedia of Genes and Genomes (KEGG) database (https://www.kegg.jp/).

Western blotting analysis

The expression levels of TGF-β1 and COL I in rabbit ear tissues were analyzed using western blotting. Total protein content was determined using a BCA assay kit (Beyotime, China) following protein extraction with a RIPA lysis kit (Beyotime, China). The proteins were separated by 10% SDS-PAGE and transferred to a PVDF membrane

at 110 V for one hour. Following an overnight incubation at 4 °C with primary antibodies (Proteintech, 1:1000), the membranes were incubated for an hour at 25 °C with secondary antibodies (HUABIO, 1:50,000). Tubulin antibodies (Beyotime, 1:1000) were employed as internal controls. Chemiluminescence signals were captured and analyzed using ImageJ software.

Statistical analysis

The data were expressed as mean ± standard deviation (SD). Statistical analysis was conducted employing one-way analysis of variance (ANOVA) with GraphPad Prism 9.0. *p*-value: n.s. means no significance, $^{*}p < 0.05$, $^{**}p < 0.01$, $^{***}p < 0.001$, $^{****}p < 0.0001$.

Results and discussion

Characterization of AA/PTP

The synthesized AA/PTP exhibited favorable dispersion properties, with a particle size of (48.9 ± 4.2) nm and a polydispersity index (PDI) of less than 0.3 (Fig. 2A). Furthermore, the zeta potential of AA/PTP was measured at (−19.5 ± 0.4) mV (Fig. 2B), indicating a stable formulation. To evaluate the ROS-responsive capability of the AA/PTP, the diameter was measured at specific time intervals following incubation with 0.5 mM H_2O_2. As illustrated in Fig. 2C, the particle size increased in a time-dependent manner, reaching approximately 300 nm after 24 h, suggesting that the AA/PTP underwent hydrolysis upon exposure to H_2O_2. TEM images revealed that the spherical micelles initially exhibited a narrow particle size distribution (Fig. 2D, left and upper right). However, after H_2O_2 treatment, the initially uniform spheroidal nanostructures exhibited significant morphological degradation, manifesting as interparticle coalescence (Fig. 2D, lower right), which may have contributed to an increase in particle size, as measured by dynamic light scattering (Malvern). The observed behavior may be attributed to the ROS-responsive nature of the TK bond, which was cleaved under ROS conditions. Additionally, the PDI increased during H_2O_2 incubation, indicating a gradual loss of uniformity in particle size distribution within the dispersion. After 24 h at room temperature, white particles were observed in the AA/PTP dispersion, indicating AA precipitation. The EE and DL of AA/PTP were (91.1 ± 1.5) % and (4.6 ± 0.4) % ($n = 6$), respectively.

Moreover, the in vitro release of AA/PTP at varying H_2O_2 concentrations was further investigated, and the time-dependent release profile is displayed in Fig. 2E. AA was slowly released from AA/PTP in PBS without H_2O_2. The release rate increased significantly with increasing H_2O_2 concentration, possibly due to the breakage of the TK bond under H_2O_2 stimulation, thereby accelerating the release of AA. This result confirmed the ROS-responsive release profile of AA/PTP, enabling it to minimize drug release in normal tissues with low ROS levels while achieving efficient release in scar tissues with a high ROS microenvironment, thereby reducing potential side effects. In summary, AA/PTP represents a novel ROS-sensitive platform with promising potential for the

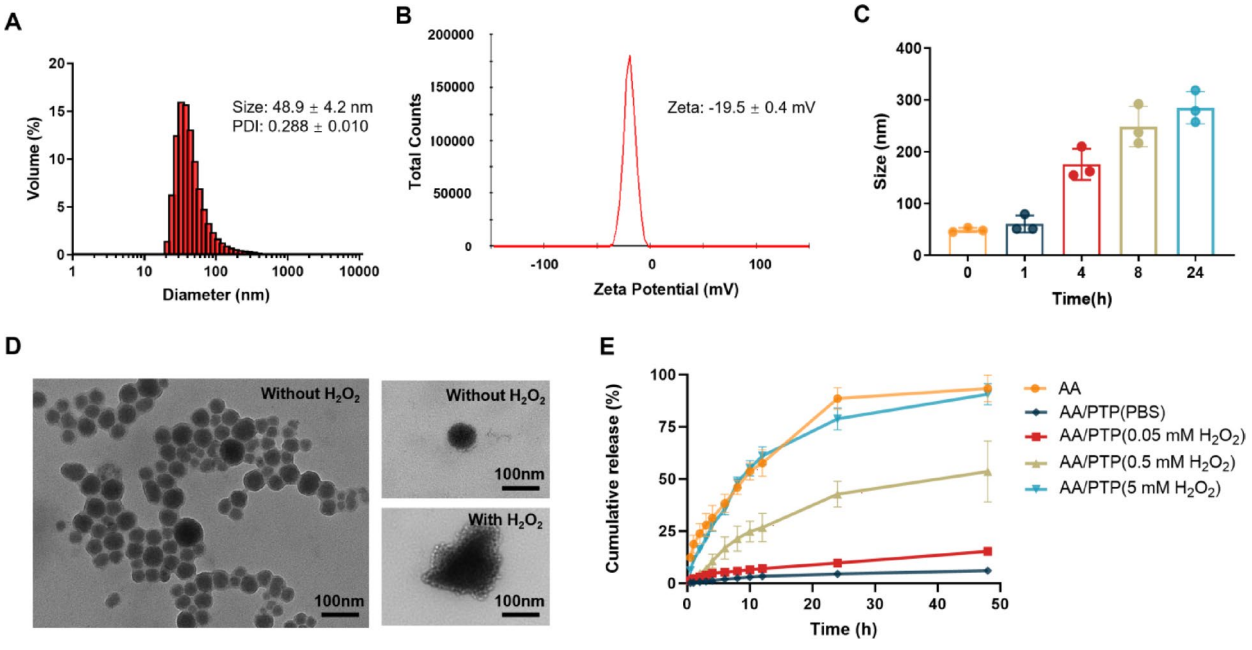

Fig. 2 Characterization of AA/PTP. (**A**) Size distributions and (**B**) zeta potentials of AA/PTP. (**C**) Particle size variations of AA/PTP at different H_2O_2 incubation durations. (**D**) Morphological changes of AA/PTP before and after H_2O_2 (0.5 mM) exposure, scale bar = 100 nm. (**E**) Drug release curves of AA after incubation with 0, 0.05, 0.5 and 5 mM H_2O_2 in PBS ($n = 5$)

targeted treatment of diseases characterized by elevated ROS levels.

Characterization and mechanical properties of AA/PTP MN patches

The AA/PTP MN patches were composed of a 10 × 10 array of regularly arranged needles (Fig. 3A). The needles exhibited a conical shape with uniform and consistent morphology (Fig. 3B). To further investigate the internal microtubule structure of the MN, the tip of a microneedle was carefully removed, and the transverse section was analyzed using FIB-SEM. As depicted in Fig. 3C, AA/PTP nanoparticles with an approximate particle size of 50 nm were observed within the microneedles, which consistent with the findings presented in Fig. 2A. Furthermore, C6-loaded nanoparticles were entrapmented onto microneedles co-loaded with rhodamine B to visualize the insertion process. Under CLSM 3D fluorescence scanning and reconstruction, green and red fluorescein were uniformly distributed across the needle surface (Fig. 3E), demonstrating the effective drug-loading capability of the microneedles. According to the HPLC results, the drug loading content was (0.48 ± 0.01) mg and (0.51 ± 0.02) mg per patch for AA MN and AA/PTP MN, respectively ($n = 6$).

HS tissue exhibited a thicker stratum corneum and a denser tissue structure compared to healthy skin. Consequently, to effectively penetrate the HS and deliver the drug to the subcutaneous tissue, sufficient mechanical strength is essential. The mechanical strength was evaluated using a texture analyzer. The MN loaded with AA/PTP has a greater mechanical strength than the blank MN, as seen in Fig. 3D. The measured force reached nearly 20 N at a displacement of 640 μm (corresponding to 80% deformation), which far exceeded the mechanical threshold required for skin penetration (0.1 N) [31]. These results demonstrated that the fabricated AA/PTP MN possessed sufficient mechanical properties to effectively pierce the stratum corneum barrier without fracture, thereby ensuring successful drug delivery.

The diffusion and release properties of drugs within the skin are directly influenced by the dissolution capacity of microneedles following skin penetration. As illustrated in Figure S1, both AA MN and AA/PTP MN completely dissolved within 10 min, facilitating subsequent drug diffusion into the skin tissue. The dissolution rate of AA/PTP MN in skin was inversely proportional to the HA concentration, with 10% HA MN dissolving completely within 2 min, while patches with 25% and 30% HA retained undissolved structures after 5 min (Figure S2). The sustained dissolution profile of HA-based microneedles in the skin prolongs drug retention at the target site, creating an optimal time window for ROS-responsive drug release. Furthermore, a high concentration of HA (such as 30%) provides the microneedle array with enhanced mechanical strength, ensuring structural integrity during skin insertion without fracture or bending, thereby guaranteeing reliable intradermal delivery. Therefore, 30% HA was selected as the optimal formulation.

To evaluate the safety profile of AA/PTP MN, the time-dependent tissue response was assessed following application to both rabbit ear HS tissue and SD rat abdominal skin. As shown in Figure S3A, the micropores on rabbit skin became less visible within 15 min. Figure S3B demonstrates that no signs of infection, such as erythema or edema, were observed after daily application of AA/PTP MN to rat abdominal skin for seven consecutive days. Furthermore, the hemolysis rate of rabbit red blood cells remained below 5% even at AA/PTP MN concentrations as high as 0.25 mM (Fig. 3F), indicating the excellent in vitro biocompatibility of AA/PTP MN.

Transdermal delivery

To evaluate the efficacy of AA/PTP MN in delivering drugs into HS tissue, the fluorescence distribution in rabbit ears was monitored after transdermal administration of C6-labeled microneedles (Fig. 3G). Owing to the dense epidermal structure of HS, the green fluorescence in the C6/PTP group was primarily restricted to the epidermis, with only minimal penetration into the dermis. In contrast, the C6/PTP MN group exhibited puncture marks in the epidermal layer, accompanied by noticeably increased fluorescence levels in both the epidermal and dermal regions, suggesting that the microneedles successfully penetrated the epidermal barrier, enabling the delivery of C6/PTP into the dermis of the HS, where they subsequently diffused. To quantify the penetration depth of AA/PTP MN, OCT was employed for real-time visualization in a rabbit ear HS model (Fig. 3H). The OCT images confirmed the formation of microchannels with a depth of approximately 800 μm, corresponding to the MN height. These channels narrowed after 10 min and remained visible in the epidermis at 30 min. The MN maintained its structural integrity without fracture during insertion, demonstrating sufficient rigidity.

Proliferation Inhibition and in vitro apoptosis of AA/PTP

Numerous malignant features of HS, including increased proliferation and excessive collagen deposition, were observed in HSFb. Consequently, inhibiting HSFb proliferation represents a promising therapeutic strategy for HS. To evaluate this, the CCK-8 assay was employed (Fig. 4A). Following incubation with free AA at concentrations ranging from 2 to 100 μM, a gradual decline in cell viability was observed. In contrast, AA/PTP exhibited varying degrees of concentration-dependent cytotoxicity. At concentrations below 10 μM, no obvious reduction in cell viability (> 90%) was noted, attributable

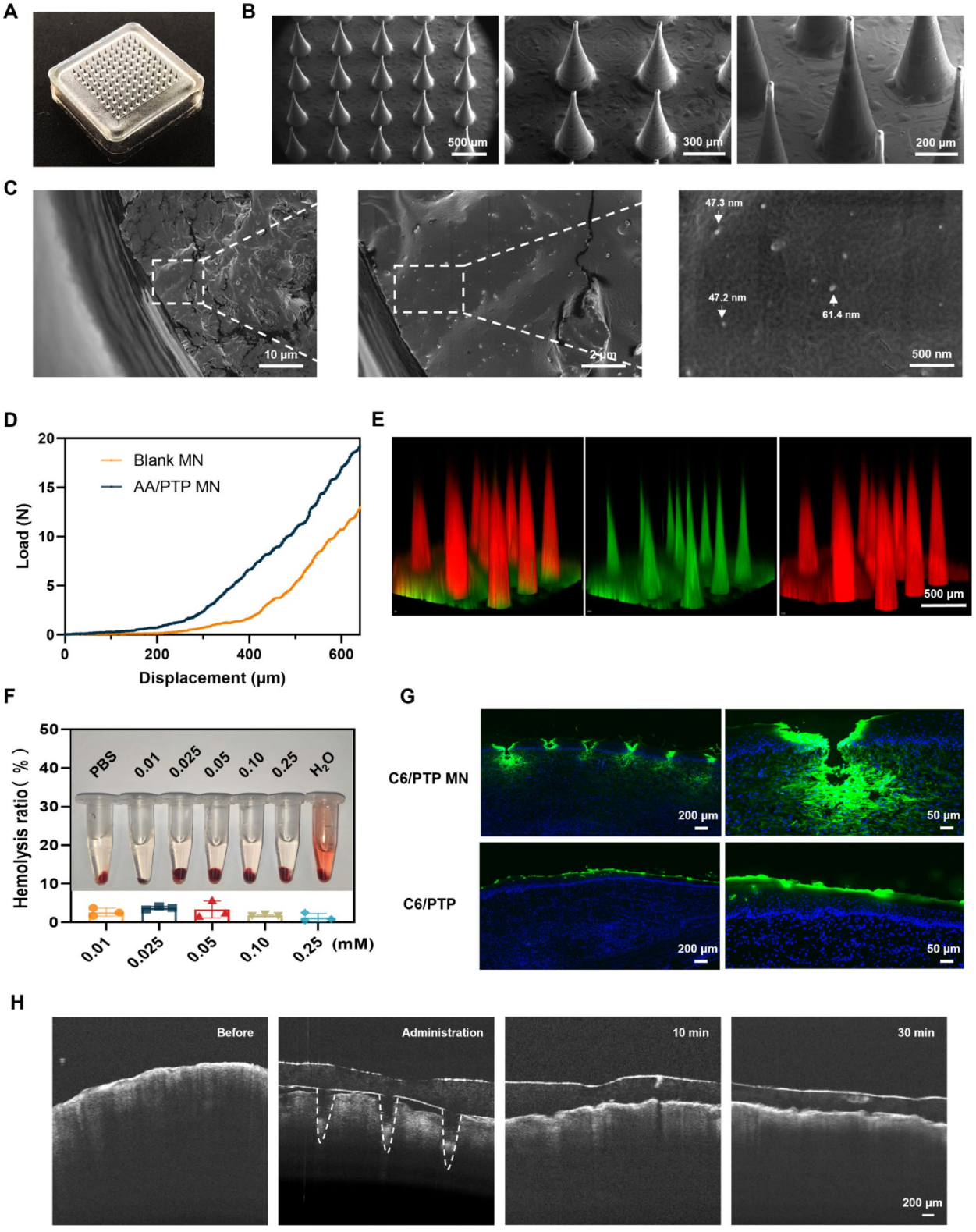

Fig. 3 Morphology, degradation and biocompatibility of AA/PTP MN patches. The morphology of the obtained MN patches characterized by (**A**) optical microscope and (**B**) FIB-SEM (scale bar = 500 μm, 300 μm, 200 μm, respectively). (**C**) The microstructure of the MN cross-section displays AA/PTP nanoparticles (white arrows, scale bar = 10 μm, 2 μm, 500 nm, respectively). (**D**) Force-displacement curves of the MN patches. (**E**) 3D fluorescence scanning and reconstruction using CLSM (Red: rhodamine B; Green: C6). (**F**) Hemolysis rates of AA/PTP MN at various concentrations ($n = 3$). (**G**) Fluorescence image of rabbit ears after transdermal administration of C6/PTP and C6/PTP MN (scale bar = 200 and 50 μm, respectively). (**H**) OCT images of insertion depth in rabbit ears (scale bar = 200 μm)

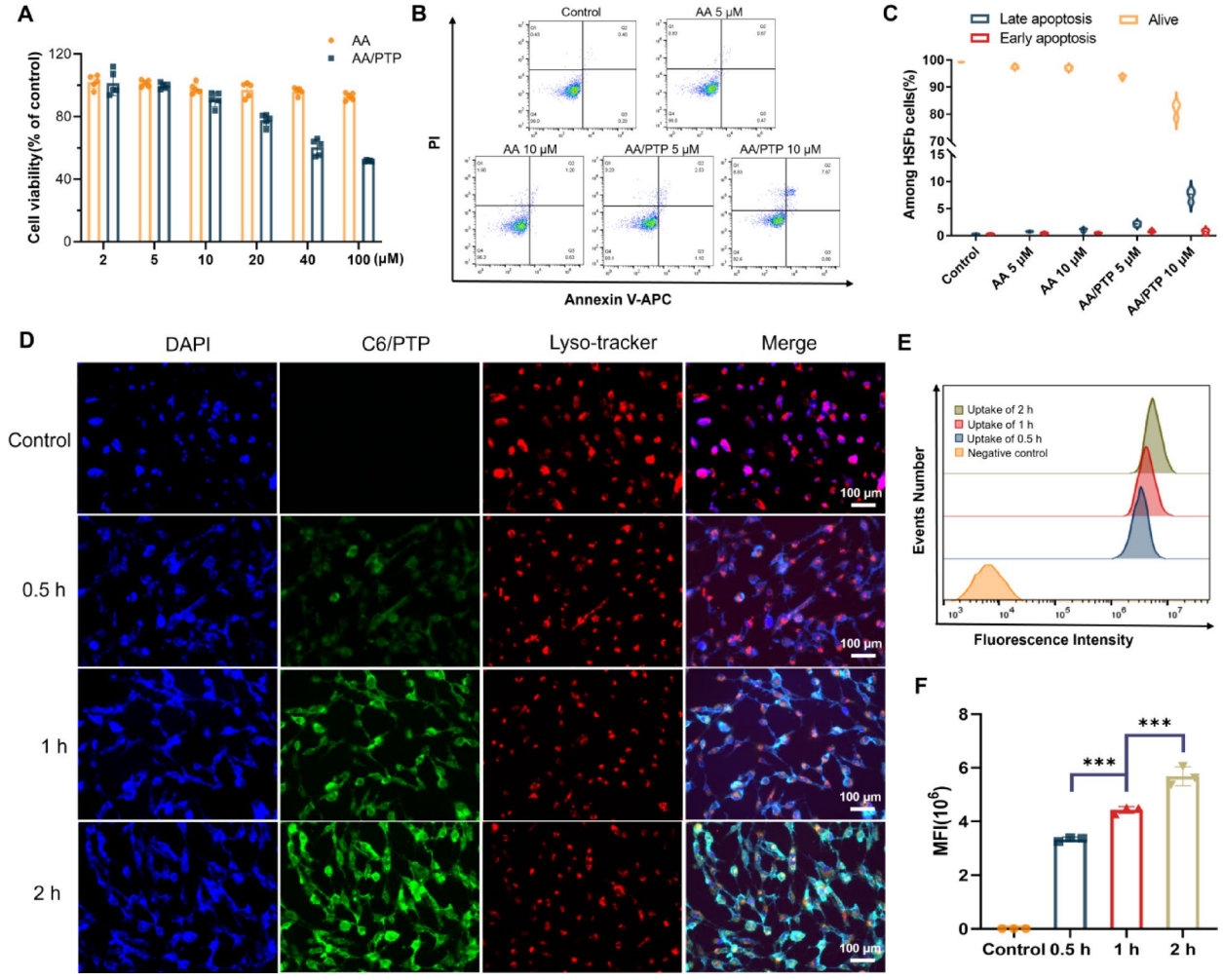

Fig. 4 Cellular internalization in HSFb. (**A**) Cytotoxicity of AA and AA/PTP in HSFb at varied concentrations by the CCK-8 assay. (**B**) Flow cytometry profiles and (**C**) quantitative evaluation of HSFb after incubation with AA or AA/PTP. (**D**) Representative fluorescence image of HSFb cultured for 0.5, 1, and 2 h with C6/PTP (green). DAPI (blue) and Lyso-Tracker Red (red) were used to stain the nuclei and lysosomes, respectively, scale bar = 100 μm. (**E**) Representative peak graph and (**F**) average fluorescence intensity in HSFb at various incubation durations performed by flow cytometry

to the excellent biocompatibility of the formulations. However, a slight reduction (about 80%) was detected at 20 μM, with significant cytotoxicity observed at higher concentrations. Similar results were obtained for Raw 264.7 (Fig. 7A). The half-maximal inhibitory concentrations (IC_{50}) for AA and AA/PTP on HSFb were 1769 μg/mL and 87.15 μg/mL, respectively, highlighting the markedly enhanced proliferation-inhibiting effect of AA/PTP on fibroblasts. Furthermore, CCK8 assays of free AA and AA/PTP in normal human primary dermal fibroblasts (HDF) and the human immortalized keratinocyte cell line HaCaT were also performed (Figure S4A and Figure S5A). At 40 μM, the cell viability of HDF was greater than or close to 80%, indicating that the anti-proliferation effect of HDF was significantly reduced compared with that of HSFb. The viability of HaCaT cells treated with both free AA and AA/PTP remained above 80% across a concentration range of 2 to 100 μM, indicating low cytotoxicity and anti-proliferation effect. It is proved that AA/PTP has a selective inhibitory effect on scar-forming fibroblasts.

To further investigate the apoptotic effects of AA/PTP, flow cytometry was employed. The cytotoxic effect of AA/PTP was more pronounced at 10 μM, with cell viability decreasing significantly to 82.6%, compared to 96.3% observed with free AA (Fig. 4B). Furthermore, the apoptotic effect of AA/PTP on HSFb was primarily observed in the late apoptotic phase (Fig. 4C). Collectively, these data demonstrated that AA/PTP holds significant promise in scar therapy.

Cellular uptake of AA/PTP

It is well established that effective cellular internalization is critical for enabling drugs to exert their intracellular functions. To visualize these processes, C6 was employed to track the nanoparticles, while Lysotracker Red dye

was used to label lysosomes. Under fluorescence microscopy, bright green fluorescence was observed following incubation with C6/PTP. The fluorescence intensity increased progressively with extended incubation time, suggesting enhanced cellular uptake efficiency (Fig. 4D). Subsequently, flow cytometry was employed to quantitatively evaluate cellular uptake. As seen in Fig. 4E-F, the fluorescence signals of cells treated with C6/PTP demonstrated a significant rightward shift in a time-dependent manner. Overall, these findings suggest that the prepared nanoparticles may substantially enhance the cellular uptake efficiency of drugs in HSFb.

In addition, we investigated the uptake characteristics of AA/PTP in Raw 264.7 cells, and the results (Figure S6A) showed that cellular uptake increased over time. The comparable fluorescence intensities observed at 30 and 60 min indicated rapid internalization, with uptake approaching saturation within 30 min.

Anti-oxidative capacity of AA/PTP in vitro

Excessive ROS levels during wound healing can cause immune dysregulation and contribute to chronicity [32]. AA is a potent antioxidant substance that has been used to scavenge excess ROS in pathological conditions such as cardiac fibrosis and osteoporosis [33, 34]. In the present study, we evaluated the anti-oxidative capacity of free AA and its ROS-responsive nanoparticle formulation (AA/PTP) in HSFb, HDF and HaCaT cells. The results showed a pronounced increase in green fluorescence following H_2O_2 stimulation, indicating successful induction of oxidative stress. Subsequent treatment with either free AA or AA/PTP significantly reduced intracellular ROS levels in all three cell lines (Fig. 5). Notably, AA/PTP exhibited a superior ROS-eliminating effect compared with free AA at equivalent concentrations. This enhanced performance can be attributed to the promoted cellular internalization of the nanoparticles, coupled with the subsequent ROS-responsive release of AA via TK bond

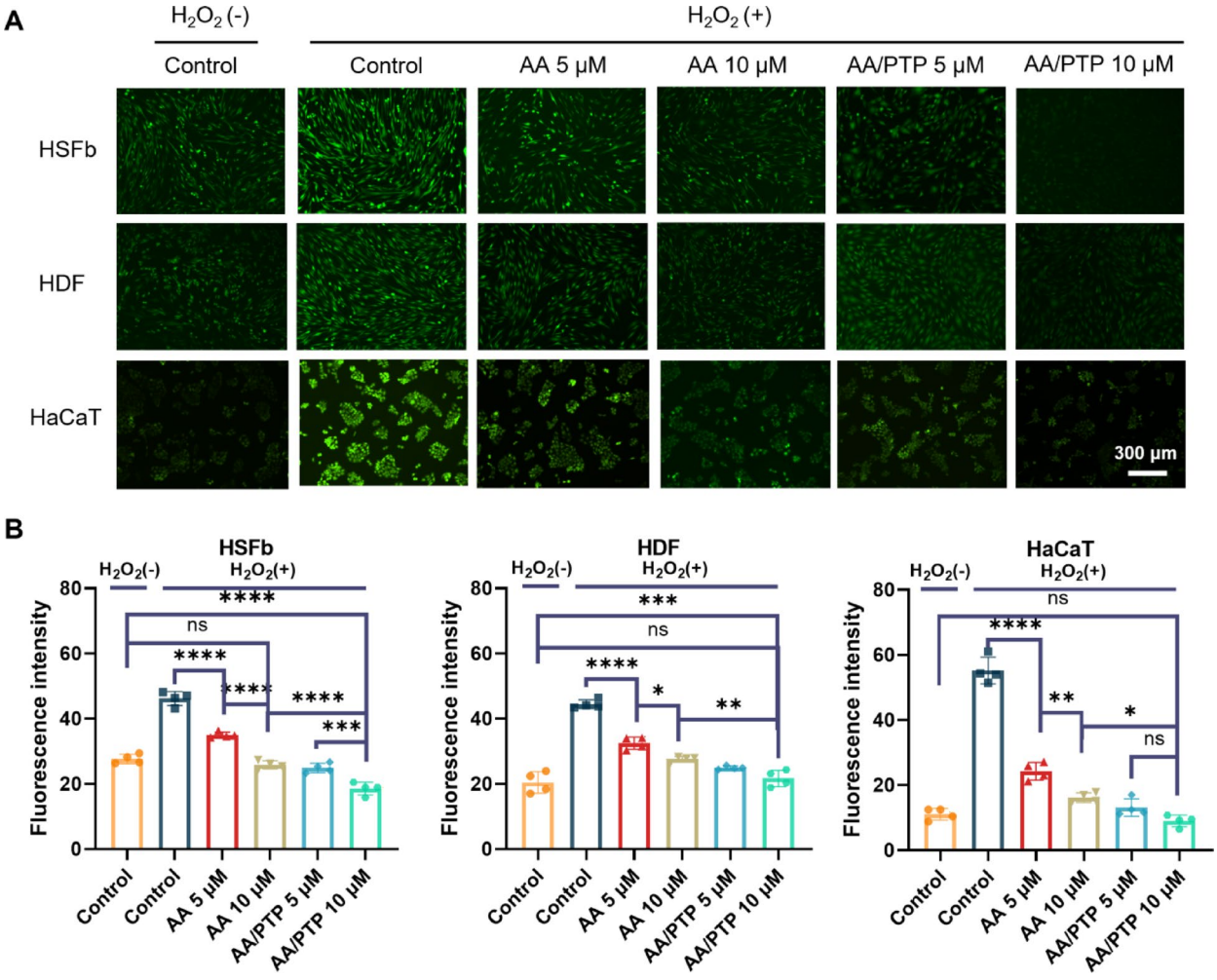

Fig. 5 Intracellular ROS scavenging of the HSFb, HDF and HaCaT. (**A**) Representative images of intracellular ROS levels in HSFb, HDF, and HaCaT cells treated with AA or AA/PTP, as well as (**B**) quantitative plots

cleavage. Importantly, under basal conditions (without H_2O_2), HSFb displayed higher initial fluorescence intensity compared to HDF cells, directly validating abnormally elevated intrinsic ROS in HS cells.

Cell migration assay

The inhibition on the migration of HSFb and macrophages was evaluated by wound scratch assay and transwell methods, respectively. As shown in Fig. 6A-B, the WHR of the control group reached 40.6% at 12 h, and was almost covered at 24 h, indicating that the growth rate of HSFb was relatively fast. Given that excessive fibroblast proliferation and migration can lead to HS, it is important to inhibit the migration of HSFb. Figure 6B showed that the WHR at AA treatment concentrations of 5 μM and 10 μM for 24 h decreased to 68.8% and 46.7% respectively. Meanwhile, the migration distance after AA/PTP treatment was further reduced, especially at 10 μM, where the WHR was only 21.1%. However, the inhibitory effect of AA/PTP on the migration of HDF and HaCaT cell lines was significantly attenuated, with a negligible impact on HaCaT proliferation (Figure S4, S5). These findings indicate that AA/PTP exerts a selective anti-proliferative effect on HSFb, with minimal impact on HDF and HaCaT cells, demonstrating favorable cell-type specificity. This characteristic helps minimize damage to surrounding normal skin during targeted treatment of HS. The selectivity of AA/PTP on HSFb over HDF and HaCaT cells may be attributed to its targeted inhibition of dysregulated signaling cascades (such as TGF-β, PI3K/Akt) [35, 36] that are hyperactive in the pathological scar fibroblasts but remain quiescent in normal skin cells.

In addition, the transwell migration assay confirmed the inhibitory effects of AA and AA/PTP on the migration and infiltration of macrophages in the HS environment (Fig. 7B-C). Collectively, our results revealed that AA/PTP significantly inhibited fibroblast formation and macrophage migration to HS tissue, ultimately yielding a scarless outcome.

In vitro mRNA expressions of collagens

The mRNA expression levels of COL I, COL III and TGF-β1 in HSFb are presented in Fig. 6C. Free AA inhibited collagen expression to some extent, with the inhibitory effect becoming more pronounced as its concentration increased. Notably, AA/PTP demonstrated a stronger inhibitory effect than free AA at lower concentrations, which may be attributed to the role of nanoparticles in promoting cellular internalization, thereby enhancing the suppression of fibrocyte activity.

Macrophage polarization and anti-inflammatory effects in vitro

Macrophages serve as pivotal regulators in HS tissue remodeling. The polarization of macrophages from the pro-inflammatory M1 to the anti-inflammatory M2 phenotype is essential for transitioning wound healing from the inflammatory phase to the regeneration phase. To investigate the effects of AA and AA/PTP on M1/M2 polarization, flow cytometry was performed to analyze the phenotypic changes in M1 (labeled with CD86) and

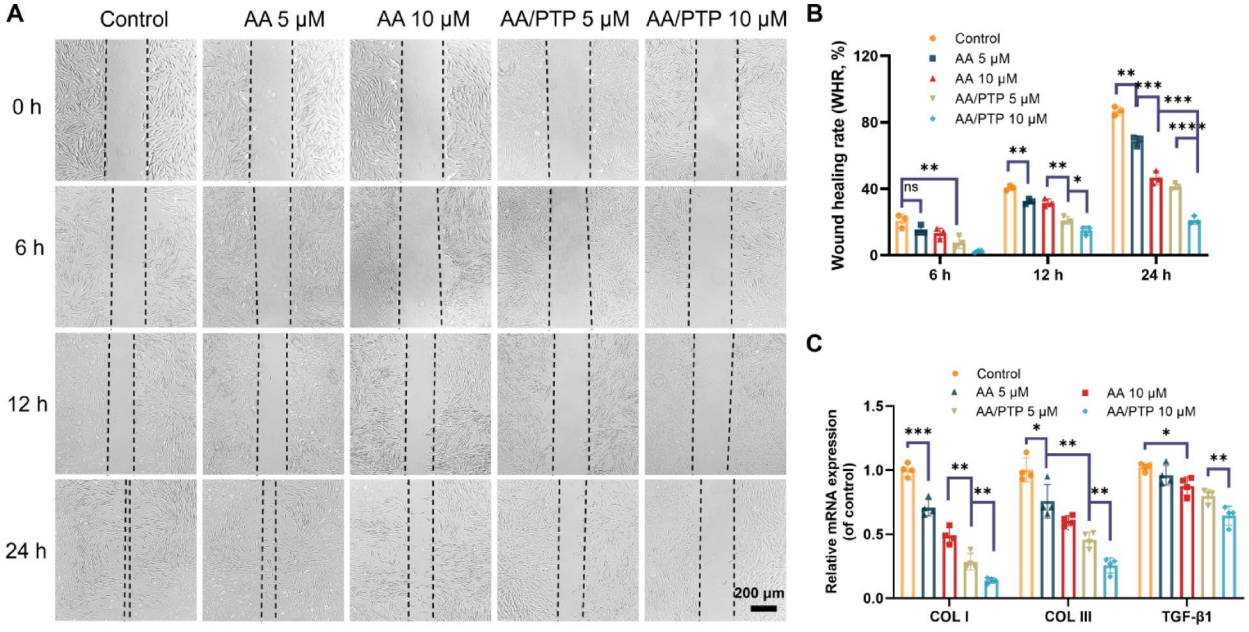

Fig. 6 Evaluation of migration activity and mRNA expression of HSFb. (**A**) Representative optical images showing the HSFb migrated toward the wound gap and (**B**) WHR in the scratch assay, scale bar = 200 μm. (**C**) The mRNA expression of COL I, COL III, and TGF-β1 was quantified by RT-PCR ($n = 4$)

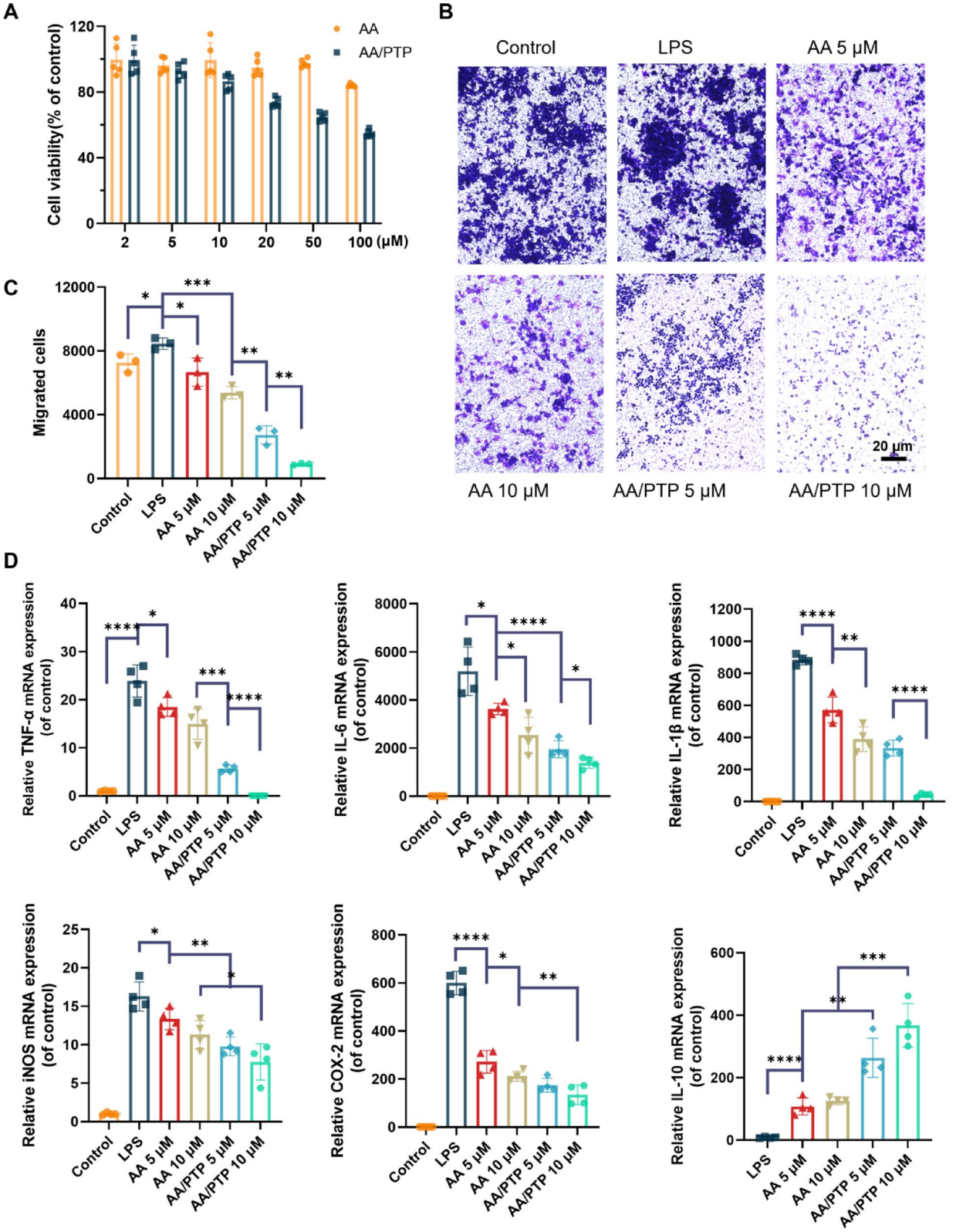

Fig. 7 Evaluation of cytotoxicity, inhibition of migration activity and mRNA expression of Raw264.7. (**A**) Cytotoxicity of AA and AA/PTP in Raw 264.7 at varied concentrations by the CCK-8 assay. (**B**) Transwell migration assay of macrophages and (**C**) semi-quantification by Image J. (**D**) The mRNA expressions of Raw 264.7 cells quantified by RT-PCR ($n = 4$)

M2 (labeled with CD206) macrophages before and after treatment. As shown in Figure S6B, treatment with AA and AA/PTP significantly reduced CD86 expression compared to the LPS-stimulated group (10 μM: 0.90 and 0.78, respectively), whereas CD206 levels were slightly elevated (10 μM: 1.12 and 1.16, respectively). These results indicate that AA/PTP markedly suppresses M1 macrophage polarization.

Sustained chronic inflammation may induce an excess of M1 macrophages, thereby exacerbating HS pathogenesis through pro-fibrotic signals [37]. As shown in Fig. 7D, the mRNA levels of inflammation-related factors in Raw 264.7 were significantly up-regulated (TNF-α, IL-6, IL-1β, iNOS, COX-2) in the presence of LPS. After treatment with AA and AA/PTP, the gene expression of these pro-inflammatory factors showed varying degrees of downregulation. Since all these markers are related to the M1 polarization of macrophages [38], these results also substantiate that AA and AA/PTP actively regulate the polarization of macrophages. Meanwhile, IL-10 plays an important role in inflammatory diseases, and its levels were significantly increased in the presence of AA and AA/PTP. Collectively, our results suggest that AA/PTP significantly suppresses M1 polarization of macrophages and has excellent anti-inflammatory effects. This may promote cell-mediated ECM remodeling and reshape the pathological microenvironment in HS.

Inhibitory efficacy of hypertrophic Scar in vivo

Similar to hypertrophic scars in humans, the rabbit ear's full-thickness incision was characterized by excessive collagen deposition with disorganized distribution, inflammation, and vascularization [39]. Figure 8A displays the timeline of different stages throughout the experiment. The HS model was successfully established by day 21, and the HS tissues were harvested on day 42. Figure 8B depicts the appearance of the HS, characterized by dark red coloration and an elevated scar surface. However, the erythema and swelling of the scar were significantly reduced following treatment with AA/PTP MN, and the scar boundary appeared smoother and more blurred compared to the other groups. In contrast, the treatment

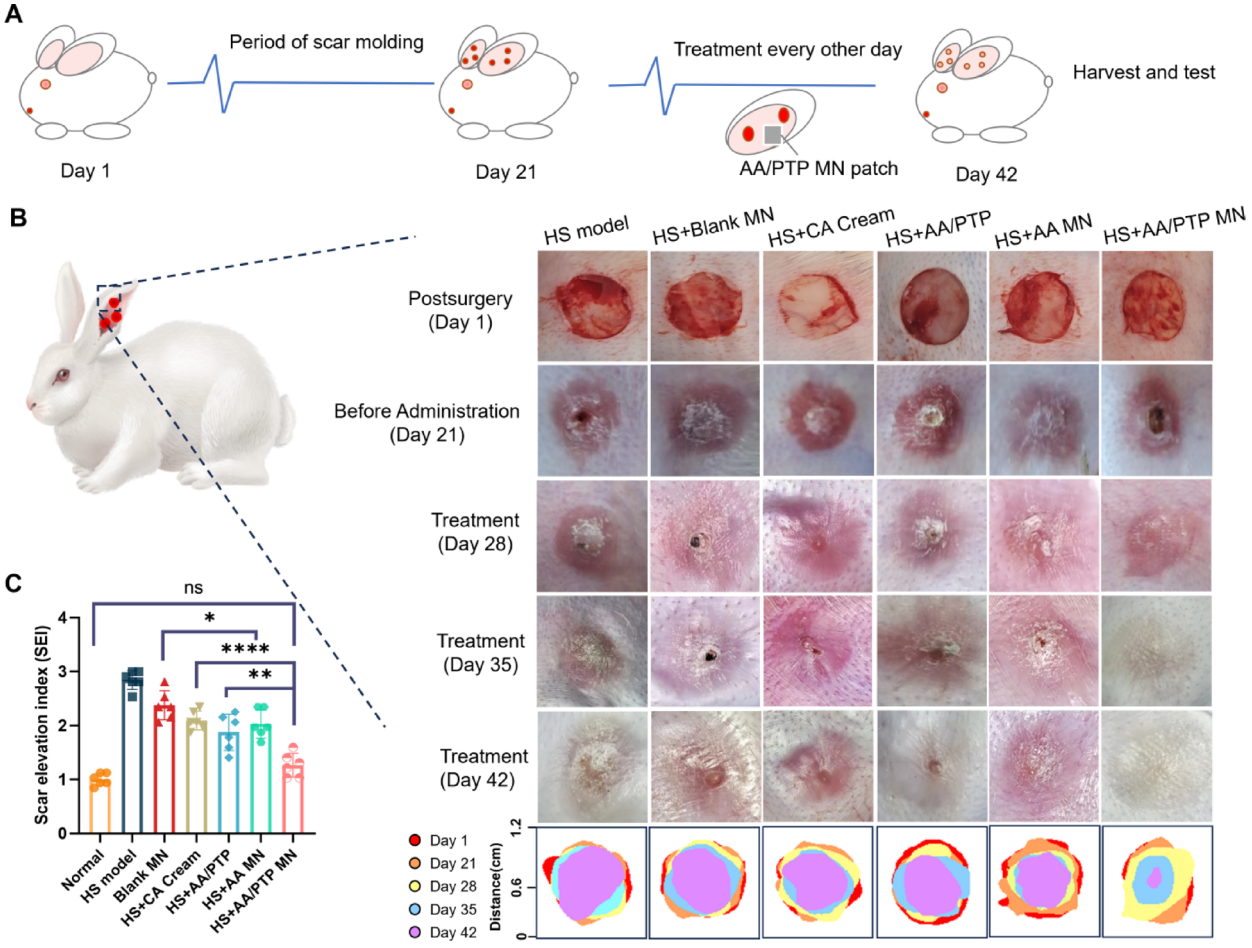

Fig. 8 Evaluation of the therapeutic effect on the rabbit HS ear under different interventions. (**A**) Time nodes for different stages throughout the experiment. (**B**) Representative photographs and closing traces of skin lesions from each group at different time intervals. (**C**) SEI value of different groups ($n = 6$)

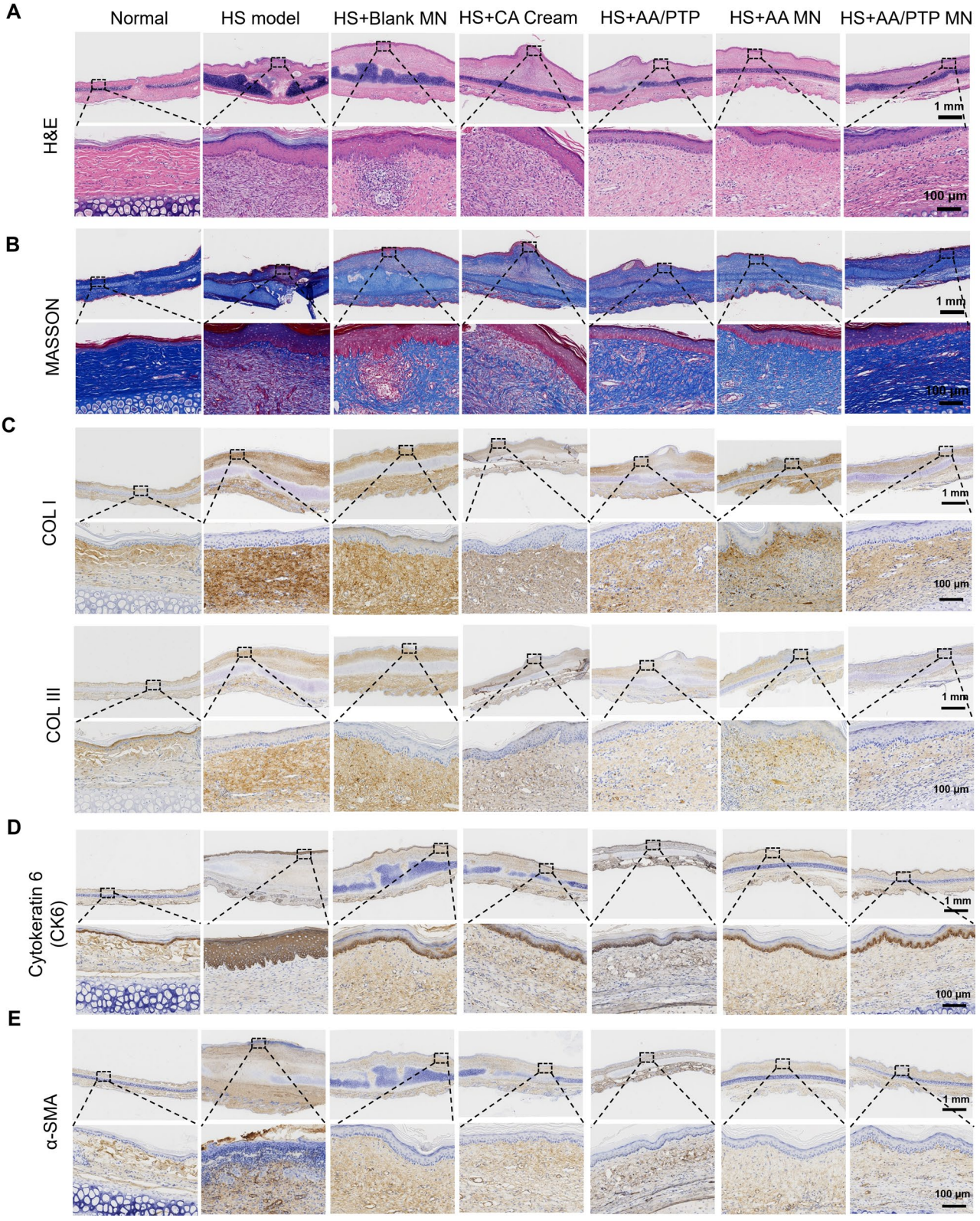

Fig. 9 Representative histological images of HS tissues stained by (**A**) H&E and (**B**) Masson after treatment with various preparations. (**C**) Immunofluorescence staining for COL I and III. Immunofluorescence staining for (**D**) Cytokeratin 6 (CK6) and (**E**) α-SMA. Scale bar = 1 mm, 100 μm, respectively

effects of the blank MN and CA cream groups were limited, with the scar texture remaining notably red.

Next, the scar elevation index (SEI) was calculated to quantitatively assess the improvement of HS (Fig. 8C), as it was found to be positively correlated with HS formation. Compared to normal skin, the HS in the model group was significantly thicker, and the SEI value increased to 2.8. After 21 days of treatment, the SEI decreased across all groups. The most notable reduction in SEI was observed in the HS + AA/PTP MN group, which reached 1.3, a value even lower than that of the HS + AA/PTP group (1.9, $p < 0.01$). In addition, no significant difference was detected between the normal group and the AA/PTP MN group. Meanwhile, the SEI of the HS + Blank MN group decreased slightly, which may be attributed to the reparative effects of the hyaluronic acid substrate and the mechanical stimulation provided by the microneedles. These findings suggest that the therapeutic efficacy of AA/PTP MN was mainly attributed to the accumulation and controlled release of AA/PTP at the HS site.

Histological and immunohistochemical analysis

As illustrated in Fig. 8A, the dermis of healthy skin appeared thin and well-defined, with neatly organized and loosely arranged collagen fibers and fibroblasts. In contrast, the epidermis and dermis of the HS group exhibited significant epithelialization, characterized by disorganized fibroblasts, irregular stratum corneum thickness, and a marked increase in inflammatory cell infiltration. Following treatment with AA/PTP MN, the epidermal thickness was significantly reduced to a level comparable to normal skin, the fibroblasts displayed a regular, parallel arrangement, and the collagen fibers were relatively loosely organized, collectively demonstrating the effective remodeling of the scar tissue towards a healthy skin phenotype. However, some cartilage thickening persisted, likely resulting from the initial damage during the modeling process. In contrast, the thickness of HS tissue in the blank MN group showed only a slight reduction.

Masson's trichrome staining and immunohistochemical staining were employed to assess excessive collagen deposition, a key indicator of HS formation. As depicted in Fig. 8B, the blue collagen fibers appeared abundant and disorganized in HS tissue, in contrast to the thin, sparse, and orderly arrangement observed in the dermis of healthy skin. After 21 days of treatment, the collagen fibers exhibited a more regular reorganization and a reduction in density. However, in the HS + Blank MN and HS + CA cream groups, a significant number of collagen fibers remained irregularly distributed. The therapeutic efficacy of the HS + AA/PTP MN group surpassed that of the HS + AA/PTP and HS + CA cream groups, likely due to complete penetration of the microneedle tips through the stratum corneum, enabling more efficient drug delivery into the dermal tissue without waste. Collagen fibers in the skin are predominantly composed of type I and type III, both of which are abnormally elevated in HS tissues [40, 41]. It has been reported that AA can inhibit the expression of TGF-β1, reduce the expression of collagen I (COL I) and collagen III (COL III), thereby reducing collagen deposition and alleviating cardiac fibrosis [33]. Immunohistochemical analysis revealed that the levels of COL I and III in the HS model group were significantly higher than those in the normal group (Fig. 8C). However, these levels were effectively reduced in all treatment groups. The therapeutic effect of AA/PTP was further enhanced by incorporating microneedles. Collectively, these findings demonstrate that AA/PTP MN effectively reduces collagen deposition and inhibits the proliferation of abnormal fibroblasts.

Keratinocytes and myofibroblasts play a pathologically active role in HS progression. Cytokeratin 6 (CK6) serves as a marker of epidermal hyperproliferation, while α-smooth muscle actin (α-SMA) identifies activated myofibroblasts. As shown in Fig. 8D-E, the expression of both CK6 and α-SMA was significantly elevated in HS tissue compared to normal skin, indicating a persistently hyperactivated state of keratinocytes and myofibroblasts. Following treatment with AA/PTP MN patches, the expression of CK6 and α-SMA was effectively reduced, demonstrating normalized epidermal activation and suppressed skin fibrosis, ultimately attenuating scar tissue hyperplasia.

Macrophage polarization and inflammatory cytokines in vivo

In a chronic wound environment, the accumulation of M1 macrophages sustains the continuous release of pro-inflammatory cytokines, including TNF-α, IL-1β, and IL-6, which perpetuate immune cell recruitment and drive hyperproliferation of both fibroblasts and keratinocytes. These processes collectively contribute to epidermal thickening accompanied by hyperkeratosis. Concurrent CD206 overexpression reflected strong profibrotic signaling, with M2 macrophages secreting cytokines such as TGF-β1, which directly promote fibroblast-to-myofibroblast differentiation, leading to excessive collagen deposition and ECM disorganization. Together, M1 and M2 macrophages maintain a deleterious inflammation-fibrosis cycle that exacerbates scar pathogenesis. In vitro migration assays confirmed that AA/PTP significantly inhibits macrophage migration and infiltration within a simulated scar microenvironment. To further assess the M1/M2 macrophage distribution in vivo, immunofluorescence staining was performed on rabbit ear HS tissues. As illustrated in Fig. 10B the model

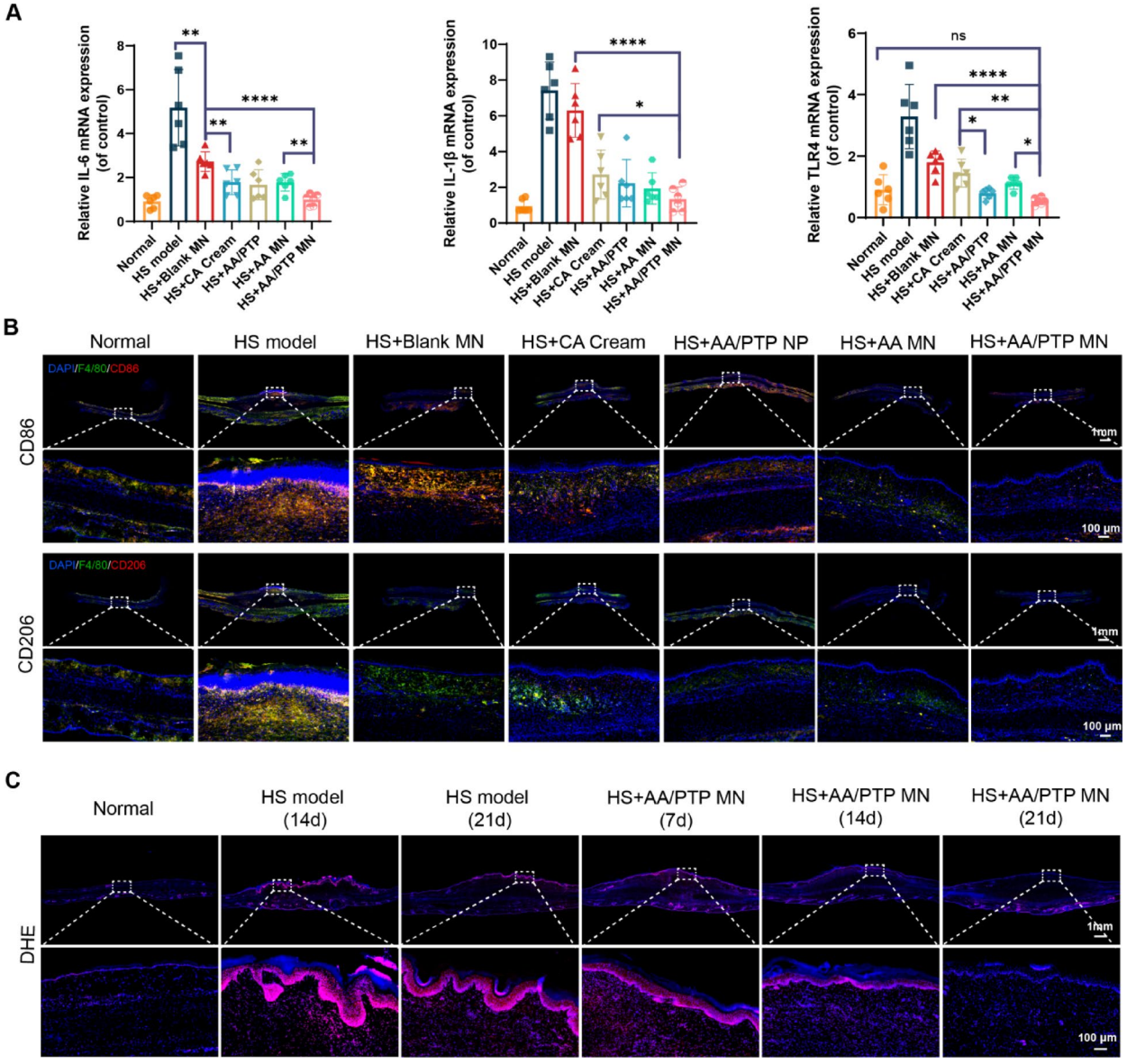

Fig. 10 Macrophage polarization, inflammatory factors and ROS levels in HS tissues of rabbit ears. (**A**) The mRNA expressions in HS tissues ($n=6$). (**B**) Immunofluorescence staining of CD68 and CD206 in HS tissues. (**C**) Immunofluorescence staining of DHE in HS tissues at different modeling processes and administration stages

group exhibited extensive macrophage infiltration in the HS tissue, with strong CD86 fluorescence intensity indicating pronounced M1 macrophage accumulation and a persistent chronic inflammatory state. Macrophage infiltration was reduced across all treatment groups, with the most pronounced decrease observed in the AA/PTP MN group, demonstrating effective suppression of pro-inflammatory signaling cascades. The simultaneous decrease in M2 macrophages indicated attenuation of pro-fibrotic signals and inhibition of fibroblast activation, ultimately shifting the HS microenvironment from chronic inflammation toward resolution and tissue homeostasis. These findings suggest that AA/PTP MN modulates inflammatory responses, thereby inhibiting the excessive proliferation of keratinocytes and fibroblasts, and ultimately promoting the restoration of the HS microenvironment.

The formation of HS is generally accompanied by inflammatory responses. IL-6 and IL-1β are important inflammatory factors that are known to stimulate the proliferation of fibroblasts and keratinocytes, resulting in epidermal thickening and exacerbating scar formation [42]. Compared with the normal group, the HS model tissue exhibited excessive inflammation, with IL-6 and IL-1β mRNA expression levels significantly elevated to 5.2 and 7.4, respectively (Fig. 10A). However, these

inflammatory factors were downregulated in the treatment groups, with the AA/PTP MN treatment group showing the least inflammatory response, indicating that macrophage M1 polarization was significantly inhibited. Toll-like receptor 4 (TLR4), an innate immune receptor, plays a critical role in stimulating the secretion of inflammatory cytokines by activating the NF-κB signaling pathway. As illustrated in Fig. 10A, TLR4 mRNA expression was markedly increased in the HS group but returned to normal levels following AA/PTP MN treatment. The therapeutic efficacy of the HS + AA/PTP MN group was significantly superior to that of the non-microneedle-assisted group ($p < 0.05$), demonstrating that microneedle-mediated delivery substantially enhanced the regulation of inflammatory factors by improving drug delivery efficiency. In addition, the anti-inflammatory effects observed in the HS + AA MN and HS + AA/PTP MN groups may be attributed to the downregulation of the TLR4/NF-κB pathway by AA, as previously reported [18], hence preventing the release of pro-inflammatory mediators, including IL-6 and IL-1β. Building upon the above findings, it can be inferred that AA/PTP further controls the excessive proliferation of keratinocytes and fibroblasts, ultimately reshaping the pathological microenvironment of HS.

Anti-oxidative effect in vivo

The in vivo ROS changes in rabbit ear tissues during HS modeling and the AA/PTP MN administration process were evaluated using dihydroethidium (DHE) staining. As shown in Fig. 10C, strong fluorescence was observed at day 14 post-modeling (one week after eschar removal), indicating that the ROS level of scar tissue was the highest in this period. This might be related to the incomplete healing of secondary trauma at the wound stage. By day 21, when the wound had fully healed and hypertrophic tissue had begun to form, ROS intensity had decreased slightly but remained substantially higher than in normal tissue. Throughout this process, continuous ROS production by myofibroblasts and chronic inflammatory infiltration collectively sustain an oxidative stress state, which consequently leads to excessive collagen deposition and scar hyperplasia. Treatment with AA/PTP MN progressively reduced the ROS levels, correlating with observed scar remission. Taken together, these findings from release kinetics (Fig. 2E), cellular assays (Fig. 5), and in vivo evaluation (Fig. 10C) provide a robust demonstration that AA/PTP MN effectively modulated the HS pathological microenvironment through reactive drug release in regions with high ROS concentrations and efficient ROS scavenging.

Collagen remodeling in HS tissue

The inhibition of scar-related mRNA expression serves as a further indicator of the therapeutic effect of HS and was assessed using RT-PCR. As illustrated in Fig. 11A, the mRNA levels of COL I and III in rabbit ear tissues across all groups corroborated the findings from Masson's trichrome staining and immunohistochemical staining (Figs. 8B-C). TGF-β1 is known to enhance myofibroblast differentiation and stimulate collagen synthesis [43]. Notably, the TGF-β1 mRNA level in HS tissue was significantly elevated, reaching levels four times higher than those in the normal group, indicating that the HS tissue remained in an active state. In contrast, HS tissues subjected to various treatments showed reduced mRNA expression levels. Specifically, the HS + AA/PTP group, HS + AA MN group, and HS + AA/PTP MN group showed a marked decline in mRNA expression. The HS + AA/PTP MN group, in particular, demonstrated mRNA levels that returned to baseline (compared to the HS group, $p < 0.0001$; compared to the normal group, *n.s.*), suggesting that the AA/PTP MN patches could effectively inhibit excessive fibroblast production, thereby preventing scar formation. The differential outcomes observed between the HS + AA MN group and the HS + AA/PTP MN group can be attributed to the design of AA/PTP in this study, which facilitated enhanced uptake by HS cells. This design improved the retention of AA within HS tissues and ultimately enhanced treatment efficacy ($p < 0.01$).

To further investigate the suppressive effects of AA/PTP MN, the protein expression levels of TGF-β1 and COL I were assessed using Western blotting. As shown in Fig. 8F, G and a considerable increase in the expression of TGF-β1 and COL I was observed in HS tissues compared to normal skin ($p < 0.001$). In addition, the expression of these proteins in the HS + Blank MN group was comparable to that in the HS model group, indicating that the blank MN had minimal impact on HS treatment. However, following treatment with AA/PTP, AA MN, and AA/PTP MN, the levels of TGF-β1 and COL I were significantly reduced ($p < 0.01$ or 0.001), with the most pronounced decrease observed in the HS + AA/PTP MN group ($p < 0.001$). The microneedle-assisted group (HS + AA/PTP MN group) demonstrated superior efficacy compared to the HA + AA/PTP group ($p < 0.01$), suggesting that the application of AA/PTP MN dramatically promoted collagen rearrangement and improved HS treatment outcomes. In addition, significant differences in TGF-β1 and COL I protein levels were observed between the HS + AA/PTP MN and the HS + CA Cream groups ($p < 0.01$ or 0.001). Moreover, no significant differences were detected between the HS + AA/PTP MN group and the normal group, highlighting the

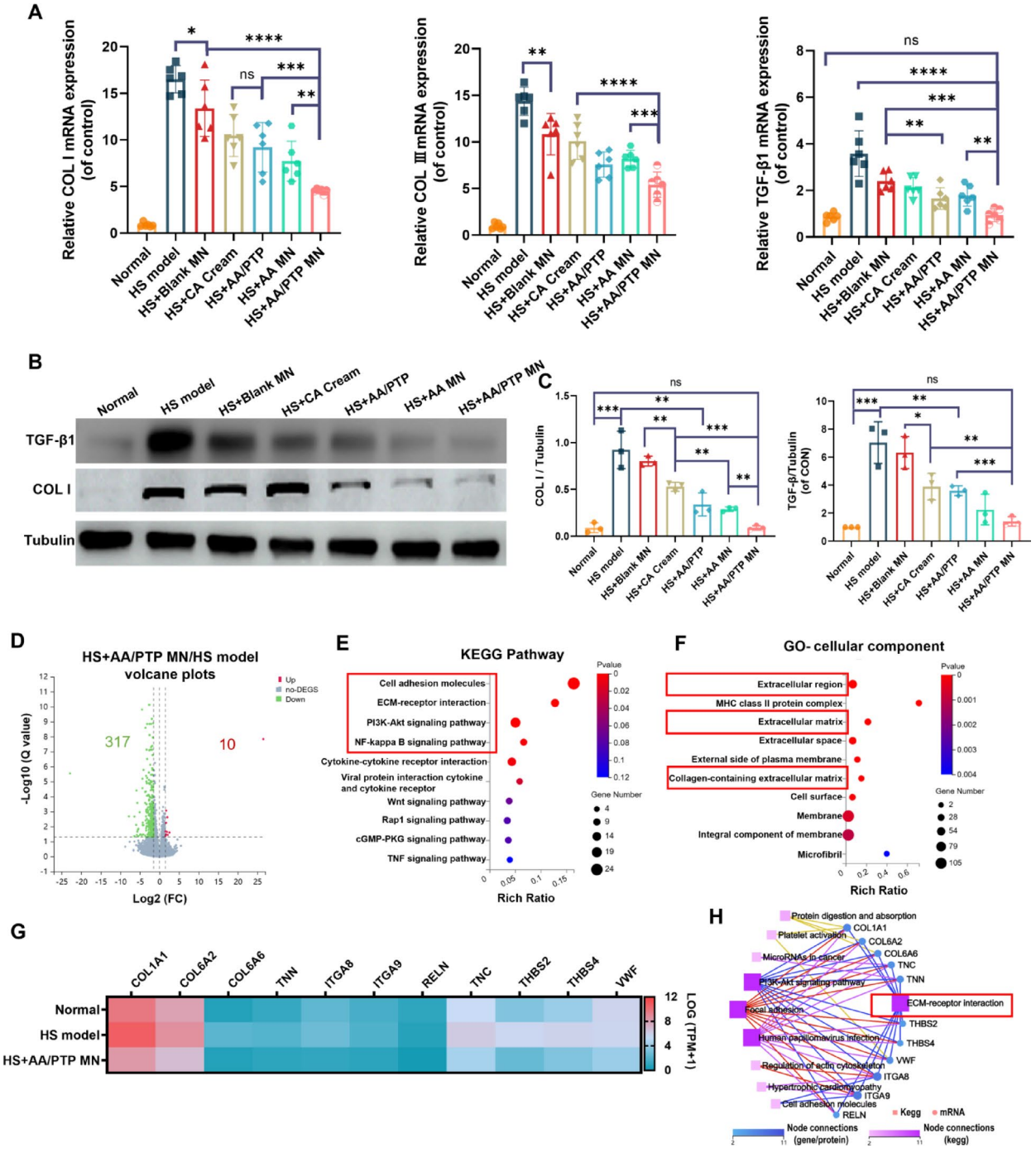

Fig. 11 Collagen expression and the gene distribution and pathway enrichment analysis in the rabbit ear HS model ($n = 3$). (**A**) The mRNA expressions in HS tissues ($n = 6$). (**B**) Western blotting of TGF-β1 and COL I in HS tissues. (**C**) Semiquantitative statistics of protein levels. (**D**) Volcano plots representing the DEGs of the HS + AA/PTP MN group against the HS group. (**E**) KEGG pathway enrichment analysis based on the down-regulated genes in AA/PTP MN treatment rabbit relative to the HS model rabbit. (**F**) Heat map of down-regulated genes involved in ECM-receptor interaction in rabbit HS models with AA/PTP MN treatment (fold change ≥ 1.5, $p < 0.05$). (**G**) The significantly enriched cellular components of Gene Ontology (GO) terms between HS + AA/PTP MN and HS groups. (**H**) KEGG pathway network of down-regulated genes involved in the ECM matrix pathway

considerable clinical potential of AA/PTP MN for the treatment of hypertrophic scars.

RNA sequencing analysis of AA/PTP MN on HS treatment

RNA sequencing was conducted on total RNA isolated from rabbit ear scar tissues. A boxplot demonstrated the global consistency of gene distribution across all samples

(Figure S7A). Volcano plots revealed 80 down-regulated and 133 up-regulated DEGs between the HS and normal groups (Figure S7B). In contrast, the HS group treated with AA/PTP MN exhibited 317 down-regulated genes and 10 up-regulated genes (Fig. 11D). KEGG pathway analysis of the DEGs indicated that ECM-receptor interactions and cell adhesion molecules play a significant role in scar formation (Figure S7C). Notably, these two pathways were also enriched among the down-regulated genes following AA/PTP MN treatment, suggesting that the therapeutic effect is primarily associated with reduced fibroblast mechanical transduction and ECM deposition (Fig. 11E). In addition, the drug-loaded MN treatment modulated the PI-3 K/Akt signaling pathway and NF-κB signaling pathway, which were closely related to the abnormal proliferation and migration of keratinocytes and the expression of inflammatory factors, respectively [44]. In summary, the therapeutic mechanism of AA/PTP MN appears to be significantly influenced by its effects on the migration and proliferation of fibroblasts and keratinocytes, as well as its regulation of inflammatory factors.

Further analysis revealed downregulation of multiple genes associated with scar formation following AA/PTP MN treatment, including *COL1A1*, *COL6A2*, *COL6A6*, *TNN*, *ITGA8*, *ITGA9*, *RELN*, *TNC*, *THBS2*, *THBS4*, and *VWF* (Fig. 11H). These genes were associated with extracellular regions (Fig. 11F), and were closely related to the ECM deposition, focal adhesion, the PI3K-Akt signaling pathway, and human papillomavirus infection (Fig. 11G). These results also confirmed that the therapeutic effect of AA/PTP MN was closely related to the regulation of fibroblasts, keratinocytes and inflammatory factors [45–51]. In conclusion, the degradation of AA/PTP MN enhanced cell-cell and cell-matrix interactions, influenced the migration of keratinocytes and fibroblasts, suppressed the NF-κB inflammatory pathway, and ultimately reduced collagen proliferation, thereby contributing to the treatment of HS.

Conclusions

In this study, a microneedle-mediated transdermal drug delivery platform (AA/PTP MN) was constructed in a minimally invasive and painless manner, providing a safe, convenient, and effective therapeutic strategy for the long-term treatment of HS. The encapsulated AA/PTP demonstrated enhanced uptake in HSFb, prolonged drug retention time in HS tissue, and achieved responsive release of ROS within the microenvironment. The fabricated AA/PTP MN successfully penetrated the rabbit ear HS model and exhibited localized therapeutic effects, as confirmed by histological analysis, RT-PCR, RNA sequencing, and Western blotting. Furthermore, we demonstrated that the drug-loaded MN could regulate collagen fiber deposition and reconstruct the pathological microenvironment in HS by inhibiting the abnormal proliferation of fibroblasts and keratinocytes, reducing ROS and the inflammatory response, and thereby enhancing therapeutic efficacy. The nano-micro platform developed in this study presents a promising alternative strategy to improve the transdermal delivery of poorly water-soluble drugs and advance therapies for skin diseases.

Supplementary Information

The online version contains supplementary material available at https://doi.org/10.1186/s12951-025-03946-2.

Supplementary Material 1.

Acknowledgements

We express our gratitude to the Scientific Research Center of Hangzhou Medical College and to all those who have provided valuable support during this study.

Author contributions

Yawen Zhang: Writing - original draft, Data curation, Methodology, Visualization, Conceptualization, Funding acquisition. Xuanyu Tang: Writing - review & editing, Investigation, Data curation, Methodology, Validation. Yijing Ma: Writing – review & editing, Formal analysis, Methodology, Supervision, Conceptualization. Yi Qiu: Writing – review & editing, Visualization, Methodology. Xiaoting Wu: Validation, Investigation. Yue Wu: Formal analysis, Supervision. Lulu Zeng: Investigation, Data curation. Lingfeng Chen: Writing – review & editing, Supervision. Haibin Wu: Supervision, Validation. Yanyan Zheng: Investigation, Supervision. Jing Xie: Investigation, Funding acquisition. Guang Liang: Supervision, Project administration. Lina Yin: Supervision, Funding acquisition, Project administration. All authors reviewed the manuscript.

Funding

This work was supported by the Medical and Health Technology Project of Zhejiang Province, China (2023KY086), Special project of Hangzhou Medical College (KYZD2023005), Basic Scientific Research Project of Hangzhou Medical College (KYYB202108) and the Major Scientific and Technological Innovation Projects of Wenzhou (ZY2021026).

Data availability

No datasets were generated or analysed during the current study.

Declarations

Ethics approval and consent to participate

All procedures involving human participants in this study were reviewed and approved by the Ethics Committee for Human Subjects Research of Wenzhou People's Hospital (Approval No. 2022 – 415). Protocols of animal experiments were permitted by the Animal Ethics Committee of Zhejiang Province (Approval No. 2021 – 266).

Consent for publication

Not applicable.

Competing interests

The authors declare no competing interests.

Author details

[1]School of Pharmacy, Hangzhou Medical College, Hangzhou 310013, P. R. China
[2]Wenzhou People's Hospital, Third Clinical College of Wenzhou Medical University, Wenzhou 325000, P. R. China

Received: 23 July 2025 / Accepted: 13 December 2025

Published online: 24 January 2026

References

1. Wang ADDINENREFLIST, Yang L, Ran J, Yang B, Zheng X, Long W, et al. Small molecular TGF-β1-inhibitor-loaded electrospun fibrous scaffolds for preventing hypertrophic scars. ACS Appl Mater Interfaces. 2017;9:32545–53.
2. Weng W, He S, Song H, Li X, Cao L, Hu Y, et al. Aligned carbon nanotubes reduce hypertrophic scar via regulating cell behavior. ACS Nano. 2018;12:7601–12.
3. Wang PH, Huang BS, Horng HC, Yeh CC, Chen YJ. Wound healing. J Chin Med Assoc. 2018;81:94–101.
4. Gholipourmalekabadi M, Khosravimelal S, Nokhbedehghan Z, Sameni M, Jajarmi V, Urbanska AM, et al. Modulation of hypertrophic scar formation using amniotic membrane/electrospun silk fibroin bilayer membrane in a rabbit ear model. ACS Biomater Sci Eng. 2019;5:1487–96.
5. Hu CH, Tseng YW, Chiou CY, Lan KC, Chou CH, Tai CS, et al. Bone marrow concentrate-induced mesenchymal stem cell conditioned medium facilitates wound healing and prevents hypertrophic scar formation in a rabbit ear model. Stem Cell Res Ther. 2019;10:275.
6. Finnerty CC, Jeschke MG, Branski LK, Barret JP, Dziewulski P, Herndon DN. Hypertrophic scarring: the greatest unmet challenge after burn injury. Lancet. 2016;388:1427–36.
7. Iosifidis C, Goutos I. Percutaneous collagen induction (microneedling) for the management of non-atrophic scars: literature review. Scars Burn Heal. 2019;5:2059513119880301.
8. Manuskiatti W, Kaewkes A, Yan C, Ng JN, Glahn JZ, Wanitphakdeedecha R. Hypertrophic Scar outcomes in fractional laser monotherapy versus fractional sssssssssLaser-Assisted topical corticosteroid delivery: A randomized clinical trial. Acta Derm Venereol. 2021;101:adv00416.
9. Brinkhaus B, Lindner M, Schuppan D, Hahn EG. Chemical, pharmacological and clinical profile of the East Asian medical plant *centella asiatica*. Phytomedicine. 2000;7:427–48.
10. Razali NNM, Ng CT, Fong LY. Cardiovascular protective effects of *centella asiatica* and its triterpenes: a review. Planta Med. 2019;85:1203–15.
11. Park KS. Pharmacological effects of centella Asiatica on skin diseases: evidence and possible mechanisms. Evid Based Complement Alternat Med. 2021;2021:5462633.
12. Lv J, Sharma A, Zhang T, Wu Y, Ding X. Pharmacological review on asiatic acid and its derivatives: a potential compound. SLAS Technol. 2018;23:111–27.
13. Somboonwong J, Kankaisre M, Tantisira B, Tantisira MH. Wound healing activities of different extracts of *centella asiatica* in incision and burn wound models: an experimental animal study. BMC Complement Altern Med. 2012;12:103.
14. Kukula O, Kırmızıkan S, Tiryaki ES, Çiçekli MN, Günaydın C. Asiatic acid exerts an anti-psoriatic effect in the imiquimod-induced psoriasis model in mice. Immunopharmacol Immunotoxicol. 2022;44:367–72.
15. Soo Lee Y, Jin DQ, Beak SM, Lee ES, Kim JA. Inhibition of ultraviolet-A-modulated signaling pathways by asiatic acid and ursolic acid in HaCaT human keratinocytes. Eur J Pharmacol. 2003;476:173–8.
16. Chen XC, Huang LF, Tang JX, Wu D, An N, Ye ZN, et al. Asiatic acid alleviates cisplatin-induced renal fibrosis in tumor-bearing mice by improving the TFEB-mediated autophagy-lysosome pathway. Biomed Pharmacother. 2023;165:115122.
17. Zhang YW, Tu LL, Zhang Y, Pan JC, Zheng GL, Yin LN. Liver-targeted delivery of Asiatic acid nanostructured lipid carrier for the treatment of liver fibrosis. Drug Deliv. 2021;28:2534–47.
18. Zhang Y, Wu Y, Yan Y, Ma Y, Tu L, Shao J, et al. Dual-Targeted Nanoparticle-in-Microparticle system for ulcerative colitis therapy. Adv Healthc Mater. 2023;12:e2301518.
19. Zhang Y, Wu Y, Yan Y, Ma Y, Tu L, Shao J, et al. Dual-targeted nanoparticle-in-microparticle system for ulcerative colitis therapy. Adv Healthc Mater. 2023. https://doi.org/10.1002/adhm.202301518.
20. Yang ZR, Suo H, Fan JW, Lv N, Du K, Ma T, et al. Endogenous stimuli-responsive separating microneedles to inhibit hypertrophic scar through remodeling the pathological microenvironment. Nat Commun. 2024;15:2038.
21. He J, Meng X, Meng C, Zhao J, Chen Y, Zhang Z, et al. Layer-by-layer pirfenidone/cerium oxide nanocapsule dressing promotes wound repair and prevents scar formation. Molecules. 2022;27:1830. https://doi.org/10.3390/molecules27061830
22. Liu B, Thayumanavan S. Mechanistic investigation on oxidative degradation of ROS-responsive thioacetal/thioketal moieties and their implications. Cell Reports Physical Science. 2020;1:100271.
23. Kim EA, Park JS, Kim MS, Jeong MY, Park HJ, Choi JH, et al. High-payload nanosuspension of centella Asiatica extract for improved skin delivery with no irritation. Int J Nanomed. 2021;16:7417–32.
24. Chen Y, Feng X, Meng S. Site-specific drug delivery in the skin for the localized treatment of skin diseases. Expert Opin Drug Deliv. 2019;16:847–67.
25. Than A, Liu C, Chang H, Duong PK, Cheung CMG, Xu C, Wang X, Chen P. Self-implantable double-layered micro-drug-reservoirs for efficient and controlled ocular drug delivery. Nat Commun. 2018;9:4433.
26. Xie Y, Wang H, Mao J, Li Y, Hussain M, Zhu J, et al. Enhanced in vitro efficacy for inhibiting hypertrophic scar by bleomycin-loaded dissolving hyaluronic acid microneedles. J Mater Chem B. 2019;7:6604–11.
27. Chi J, Zhang X, Chen C, Shao C, Zhao Y, Wang Y. Antibacterial and angiogenic Chitosan microneedle array patch for promoting wound healing. Bioact Mater. 2020;5:253–9.
28. Li W, Terry RN, Tang J, Feng MR, Schwendeman SP, Prausnitz MR. Rapidly separable microneedle patch for the sustained release of a contraceptive. Nat Biomed Eng. 2019;3:220–9.
29. Lee K, Song HB, Cho W, Kim JH, Kim JH, Ryu W. Intracorneal injection of a detachable hybrid microneedle for sustained drug delivery. Acta Biomater. 2018;80:48–57.
30. Zhang Q, Shi L, He H, Liu X, Huang Y, Xu D, Yao M, Zhang N, Guo Y, Lu Y, et al. Down-Regulating Scar formation by microneedles directly via a mechanical communication pathway. ACS Nano. 2022;16:10163–78.
31. Zhu DD, Chen BZ, He MC, Guo XD. Structural optimization of rapidly separating microneedles for efficient drug delivery. J Ind Eng Chem. 2017;51:178–84.
32. Ye Y, Zhong H, Huang S, Lai W, Huang Y, Sun C, Zhang Y, Zheng S. Reactive oxygen species scavenging hydrogel regulates stem cell behavior and promotes bone healing in osteoporosis. Tissue Eng Regen Med. 2023;20:981–92.
33. Meng Z, Li HY, Si CY, Liu YZ, Teng S. Asiatic acid inhibits cardiac fibrosis throughNrf2/HO-1 and TGF-β1/Smads signaling pathways in spontaneous hypertension rats. Int Immunopharmacol. 2019;74:105712.
34. Chen X, Han D, Liu T, Huang C, Hu Z, Tan X, Wu S. Asiatic acid improves high-fat-diet-induced osteoporosis in mice via regulating SIRT1/FOXO1 signaling and inhibiting oxidative stress. Histol Histopathol. 2022;37:769–77.
35. Shang RY, Yang JC, Hu WG, Xiao R, Hu DS, Lin ZC, et al. Artesunate attenuates skin hypertrophic scar formation by inhibiting fibroblast activation and EndMT of vascular endothelial cells. Phytomedicine. 2025;140:156498.
36. Li Z, Zhang L, Wang Y, Zhu Y, Shen H, Yuan J, et al. LA-peptide hydrogel-regulation of macrophage and fibroblast fates and their crosstalk via attenuating TGF-β to promote scarless wound healing. Bioact Mater. 2025;47:417–31.
37. Mao J, Chen L, Cai Z, Qian S, Liu Z, Zhao B, et al. Advanced biomaterials for regulating polarization of macrophages in wound healing. Adv Funct Mater. 2022;32:2111003.
38. Lu G, Zhang R, Geng S, Peng L, Jayaraman P, Chen C, Xu F, Yang J, Li Q, Zheng H, et al. Myeloid cell-derived inducible nitric oxide synthase suppresses M1 macrophage polarization. Nat Commun. 2015;6:6676.
39. Zhang J, Zheng Y, Lee J, Hua J, Li S, Panchamukhi A, Yue J, Gou X, Xia Z, Zhu L, Wu X. A pulsatile release platform based on photo-induced imine-crosslinking hydrogel promotes scarless wound healing. Nat Commun. 2021;12:1670.
40. Tejiram S, Zhang J, Travis TE, Carney BC, Alkhalil A, Moffatt LT, et al. Compression therapy affects collagen type balance in hypertrophic scar. J Surg Res. 2016;201:299–305.
41. Lin S, Quan G, Hou A, Yang P, Peng T, Gu Y, et al. Strategy for hypertrophic scar therapy: improved delivery of triamcinolone acetonide using mechanically robust tip-concentrated dissolving microneedle array. J Control Release. 2019;306:69–82.
42. Li ZJ, Kim SM. The application of the starfish hatching enzyme for the improvement of scar and keloid based on the fibroblast-populated collagen lattice. Appl Biochem Biotechnol. 2014;173:989–1002.
43. Penn JW, Grobbelaar AO, Rolfe KJ. The role of the TGF-β family in wound healing, burns and scarring: a review. Int J Burns Trauma. 2012;2:18–28.
44. Bran GM, Goessler UR, Hormann K, Riedel F, Sadick H. Keloids: current concepts of pathogenesis (review). Int J Mol Med. 2009;24:283–93.
45. Theocharidis G, Drymoussi Z, Kao AP, Barber AH, Lee DA, Braun KM, Connelly JT. Type VI collagen regulates dermal matrix assembly and fibroblast motility. J Invest Dermatol. 2016;136:74–83.
46. Castagnaro S, Chrisam M, Cescon M, Braghetta P, Grumati P, Bonaldo P. Extracellular collagen VI has prosurvival and autophagy instructive properties in mouse fibroblasts. Front Physiol. 2018;9:1129.

47. Xiang W, Guo Z, Zhang Y, Xu Y. The role of Tenascin-C in hypertrophic scar formation: insights from cell and animal experiments. Clin Cosmet Investig Dermatol. 2024;17:1637–48.
48. 48, Albacete-Albacete L, Sánchez-Álvarez M, Del Pozo MA. Extracellular vesicles: an emerging mechanism governing the secretion and biological roles of Tenascin-C. Front Immunol. 2021;12:671485.
49. Klaas M, Mäemets-Allas K, Heinmäe E, Lagus H, Cárdenas-León CG, Arak T, Eller M, Kingo K, Kankuri E, Jaks V. Thrombospondin-4 is a soluble dermal inflammatory signal that selectively promotes fibroblast migration and keratinocyte proliferation for skin regeneration and wound healing. Front Cell Dev Biol. 2021;9:745637.
50. Griffin MF, desJardins-Park HE, Mascharak S, Borrelli MR, Longaker MT. Understanding the impact of fibroblast heterogeneity on skin fibrosis. Dis Model Mech 2020;13:dmm044164.
51. Zhao X, Kwan JYY, Yip K, Liu PP, Liu FF. Targeting metabolic dysregulation for fibrosis therapy. Nat Rev Drug Discov. 2020;19:57–75.

Publisher's note